Amyloid-like aggregates cause lysosomal defects in neurons via gain-of-function toxicity

Irene Riera-Tur[1,2,*], Tillman Schäfer[3,10,*], Daniel Hornburg[4,5,11,*], Archana Mishra[1], Lorena Fernández-Mosquera[6], Dennis Feigenbutz[1,2], Patrick Auer[1,2], Matthias Mann[4], Wolfgang Baumeister[3], Rüdiger Klein[1], Felix Meissner[5], Nuno Raimundo[7], Rubén Fernández-Busnadiego[3,8,9,#] and Irina Dudanova[1,2,#]

[1]Department of Molecules – Signaling – Development, Max Planck Institute of Neurobiology, Martinsried, Germany

[2]Molecular Neurodegeneration Group, Max Planck Institute of Neurobiology, Martinsried, Germany

[3]Department of Molecular Structural Biology, Max Planck Institute of Biochemistry, Martinsried, Germany

[4]Department of Proteomics and Signal Transduction, Max Planck Institute of Biochemistry, Martinsried, Germany

[5]Experimental Systems Immunology Group, Max Planck Institute of Biochemistry, Martinsried, Germany

[6]The William Harvey Research Institute, Barts and The London School of Medicine and Dentistry, Queen Mary University of London, London, UK

[7]Department of Cellular and Molecular Physiology, Penn State College of Medicine, Hershey, PA, USA

[8]Institute of Neuropathology, University Medical Center Goettingen, Goettingen, Germany

[9]Cluster of Excellence "Multiscale Bioimaging: from Molecular Machines to Networks of Excitable Cells" (MBExC), University of Goettingen, Goettingen, Germany

[10]Current affiliation: Cryo-EM Facility, Max Planck Institute of Biochemistry, Martinsried, Germany

[11]Current affiliation: Department of Genetics, Stanford University School of Medicine, Stanford, CA, USA

*These authors contributed equally

#These authors contributed equally

Correspondence:

ruben.fernandezbusnadiego@med.uni-goettingen.de (R.F.-B.), idudanova@neuro.mpg.de (I.D.)

Abstract

The autophagy-lysosomal pathway is impaired in many neurodegenerative diseases characterized by protein aggregation, but the link between aggregation and lysosomal dysfunction remains poorly understood. Here, we combine cryo-electron tomography, proteomics and cell biology studies to investigate the effects of protein aggregates in primary neurons. We use artificial amyloid-like β-sheet proteins (β proteins) to focus on the gain-of-function aspect of aggregation. These proteins form fibrillar aggregates and cause neurotoxicity. We show that late stages of autophagy are impaired by the aggregates, resulting in lysosomal alterations reminiscent of lysosomal storage disorders. Mechanistically, β proteins interact with and sequester AP-3μ1, a subunit of the AP-3 adaptor complex involved in protein trafficking to lysosomal organelles. This leads to destabilization of the AP-3 complex, missorting of AP-3 cargo, and lysosomal defects. Restoring AP-3μ1 expression ameliorates neurotoxicity caused by β proteins. Altogether, our results highlight the link between protein aggregation and neurotoxicity, pointing to lysosomes as particularly vulnerable organelles.

Keywords: protein aggregation, neurodegeneration, autophagy-lysosomal pathway, cryo-electron tomography, mass spectrometry

Introduction

The autophagy-lysosomal system is a major cellular degradation pathway for long-lived proteins, macromolecular complexes and damaged organelles (Finkbeiner, 2019; Settembre et al., 2013). Defects in this system cause a number of severe disorders known as lysosomal storage diseases, often characterized by early-onset neurodegeneration (Fraldi et al., 2016; Platt et al., 2018). In addition, lysosomal function is compromised in many age-related neurodegenerative disorders, such as amyotrophic lateral sclerosis, Alzheimer's, Parkinson's and Huntington's disease (Abeliovich and Gitler, 2016; Finkbeiner, 2019; Fraldi et al., 2016; Nixon, 2020; Taylor et al., 2016; Wang et al., 2018). Another convergent feature of late-onset neurodegenerative diseases is protein misfolding and aggregation, which leads to accumulation of toxic protein species and neuronal demise (Soto and Pritzkow, 2018). As autophagy represents an important pathway for removal of aggregated proteins, dysfunction of the autophagy-lysosomal system facilitates the build-up of aggregates (Finkbeiner, 2019; Wang et al., 2018). Conversely, aggregating proteins themselves might directly interfere with the normal function of the autophagy-lysosomal machinery (Cuervo et al., 2004; Winslow et al., 2010; Wong and Holzbaur, 2014). However, until now the mechanistic link between aggregation and lysosomal impairments is not completely understood.

One difficulty in studying the role of protein aggregation in cellular dysfunction is the overlap of gain- and loss-of-function effects resulting from protein misfolding. On one hand, reduction in the cellular pool of the correctly folded form of an aggregating protein results in a partial loss of its native function. At the same time, the misfolded conformation of the protein can engage in aberrant interactions with cellular membranes and with other proteins, causing gain-of-function toxicity (Bauerlein et al., 2017; Chiti and Dobson, 2017; Kim et al., 2016; Olzscha et al., 2011; Winner et al., 2011; Yang and Hu, 2016). These loss- and gain-of-function effects occur in parallel and are difficult to disentangle, especially since the native functions of many aggregating proteins are still poorly understood (Brothers et al., 2018; Saudou and Humbert, 2016; Winklhofer et al., 2008). To overcome this challenge, here we take advantage of artificial proteins (hereafter β proteins), which have been rationally designed to form antiparallel β-sheets due to an alternating pattern of polar and non-polar amino acid residues (West et al., 1999). Antiparallel β-sheet structure is an important general property of natural aggregating proteins, as demonstrated for Aβ, polyQ proteins, pathological tau and α-synuclein (Chiti and Dobson, 2017; Hartl,

2017). β proteins spontaneously assemble into amyloid-like fibrils *in vitro* (West et al., 1999). When expressed in cells, β proteins form inclusions and compromise cellular viability (Frottin et al., 2019; Olzscha et al., 2011; Vincenz-Donnelly et al., 2018; Woerner et al., 2016). Importantly, while being structurally similar to natural amyloids, β proteins do not possess any biological function, and therefore provide an excellent tool to investigate toxic gain-of-function effects of aggregation in the absence of any loss-of-function phenomena.

In this study, we use a combination of cryo-electron tomography (cryo-ET), proteomics, and cell-biological approaches to study the impact of β proteins on primary neurons. We find that β protein aggregation impairs autophagy, leads to accumulation of enlarged lysosomes with undigested cargo, and induces neurotoxicity. Our data suggest that these defects are mediated, at least in part, by the sequestration of a subunit of the AP-3 adaptor complex within the aggregates. Taken together, our findings link lysosomal impairments to toxic gain-of-function of protein aggregates.

Results

β protein aggregation causes toxicity in primary neurons

To investigate the effects of β protein aggregation in neurons, we used two β proteins, β4 and β23, which differ in primary amino acid sequence, but adopt similar β-sheet structures (West et al., 1999). The proteins were tagged with a myc epitope and fused to mCherry (β4-mCherry and β23-mCherry). We expressed β proteins in dissociated murine cortical cultures using transfection or lentiviral transduction. Upon transfection of β4-mCherry and β23-mCherry, we observed formation of abundant cytoplasmic aggregates of irregular shape (Fig. 1a-b). To assess whether the presence of β proteins caused toxicity, we stained transfected cultures for the apoptotic marker cleaved caspase-3 (Fig. 1c). Both β4-mCherry and β23-mCherry induced a significant increase in the number of cleaved caspase-3 positive cells at DIV 10+3 (Fig. 1d). We observed similar results with lentivirally transduced neurons, where both β4-mCherry and β23-mCherry aggregated and accumulated in the insoluble fraction from DIV 10+4 (Supplementary Fig. S1a-c). Significant toxicity was observed for both β proteins from DIV 10+6 onwards, corresponding to appearance of abundant aggregates (Supplementary Fig. S1d).

We further assessed dendritic complexity, as it can be affected by pathological aggregates (May et al., 2014). These experiments were performed on transfected hippocampal neurons because of their uniform morphology. Sholl analysis revealed a significant reduction in dendritic complexity in neurons transfected with either β4-mCherry or β23-mCherry (Fig. 1e-f). Altogether, these data indicate that β proteins can be used as a tool to explore the effects of protein misfolding and aggregation in neuronal cells.

Ultrastructure of neuronal β protein aggregates

We employed cryo-ET to elucidate the mechanism of β protein toxicity in neurons. This technique allows investigating the structure of protein aggregates and their impact on the cellular milieu in close-to-native conditions at molecular resolution (Bauerlein et al., 2017; Gruber et al., 2018; Guo et al., 2018; Trinkaus et al., 2021; Wagner et al., 2017). Primary cortical neurons were grown on electron microscopy (EM) grids, transfected with β proteins, and vitrified by plunge-freezing. Cryo-correlative microscopy allowed targeting the aggregates for cryo-focused ion beam (cryo-FIB) milling (Rigort et al., 2012) and subsequent cryo-ET using a Volta phase plate (Danev et al., 2014) (Supplementary Fig. S2).

Analysis of cryo-electron tomograms revealed that all β protein aggregates displayed fibrillar morphology (Supplementary Table S1) and consisted of an apparently disordered network of very thin fibrils (β4-mCherry, 4.1 ± 1.6 nm; β23-mCherry, 3.6 ± 1.1 nm in diameter; n = 30 fibrils in both cases; unpaired t-test, n. s.) (Fig. 2). The fibrils were highly curved and branched, similar to those observed *in vitro* (Olzscha et al., 2011). The fibrillar network encapsulated additional electron-dense structures that may correspond to cellular proteins sequestered by the aggregates (Olzscha et al., 2011; Woerner et al., 2016), such as ribosomes (Fig. 2). No substantial differences were observed between neuronal aggregates of β4-mCherry and β23-mCherry, or between aggregates found in neurons and in HeLa cells (Fig. 2, Supplementary Fig. S3 and Supplementary Table S1).

β protein aggregates were often found in direct contact with cellular membranes, especially those of the endoplasmic reticulum (ER) (Fig. 2, Supplementary Fig. S3 and S4f). In some cases, ER tubes surrounded the aggregate periphery and tunnelled through its interior (Supplementary Fig. S4f), similar to previous observations for polyQ, α-Synuclein and heat-shock induced aggregates (Bauerlein et al., 2017; Gruber et al., 2018; Trinkaus et al., 2021; Wagner et al., 2017). However, in contrast to polyQ fibrils (Bauerlein et al., 2017), β protein fibrils did not appear to deform cellular membranes (Supplementary Fig. S3a, c). The ER around the aggregates often engaged in membrane contact sites with mitochondria (Supplementary Fig. S3b, d), as observed for stress-induced and polyQ aggregates (Gruber et al., 2018; Zhou et al., 2014). Altogether, the morphology and cellular interactions of β protein aggregates were reminiscent of those formed by natural aggregating proteins.

β protein expression leads to defects of lysosomal morphology

Besides the presence of aggregates, the most striking ultrastructural feature of β protein-expressing neurons was the accumulation of large endo-lysosomal organelles (Fig. 3 and Supplementary Fig. S4). In control cells, a variety of endo-lysosomes was observed, including tubular early endosomes, multivesicular bodies and autolysosomes containing membranous cargo (Fig. 3a-b and Supplementary Fig. S4a-c). While all those species were also found in β protein-expressing cells, large (>1 µm in diameter) cargo-loaded autolysosomes were enriched. No β protein aggregates were observed within these organelles in tomograms or lamella overview images (Supplementary Table S1). Instead,

autolysosomes often contained extensive stacks of parallel membranes and smaller vesicles, together with an electron-dense lumen suggestive of a high protein concentration (Fig. 3c-d and Supplementary Fig. S4d). Interestingly, similar structures were reported in conditions of impaired lysosomal degradation (Abraham et al., 1968; Fernandez-Mosquera et al., 2019; Spaet et al., 1983).

Consistently with cryo-ET, light microscopy experiments with LysoTracker-loaded neurons showed that β protein expression led to an increase in lysosomal size (Fig. 4a-b). Compared to mCherry cells, lysosomes with a diameter larger than 1 µm were ~3.5-fold more abundant in both β4-mCherry and β23-mCherry cells. However, the total number of LysoTracker-positive puncta per cell was reduced (Fig. 4c). In agreement with cryo-ET findings, no significant colocalization was observed between β protein aggregates and LysoTracker-positive organelles (Fig. 4d). In summary, our cryo-ET and light microscopy data show that β protein aggregation leads to the accumulation of enlarged, cargo-rich autolysosomes, although the aggregates themselves do not appear to build up inside these organelles. This is compatible with a scenario in which autophagic cargo is successfully delivered to lysosomes, but lysosomal degradation is defective.

β proteins impair the autophagy-lysosomal pathway

To assess possible dysfunctions of the autophagy-lysosomal pathway, we estimated autophagic flux by monitoring LC3-II, an autophagy-related protein that is itself degraded by lysosomes. First, we quantified LC3-II turnover in β23-mCherry transfected HeLa cells (Fig. S5a) in the presence and absence of 50 µM chloroquine, which blocks lysosomal degradation by increasing lysosomal pH (Poole and Ohkuma, 1981). In control mCherry cells, application of chloroquine resulted in a significant, two-fold increase in LC3-II, whereas no significant accumulation of LC3-II occurred in β23-mCherry cells (Fig. 5a-b). Accordingly, the ratio of LC3-II levels with and without chloroquine was significantly reduced in β23-mCherry cells (Fig. 5c), indicative of a partial block in the autophagy-lysosomal pathway.

Second, we assessed autophagic flux in primary neurons with the help of a tandem mCherry-GFP-LC3 reporter (Leeman et al., 2018). In the low pH conditions of functional lysosomes, the GFP fluorescence of the reporter is quenched and the organelles appear red. In contrast, less acidic organelles are marked with both GFP and mCherry and appear yellow (Fig. 5d). For these experiments, we used myc-tagged

β4 protein not fused to mCherry (from here on myc-β4). A rationally designed α-helical protein with similar amino acid composition (myc-α-S824) (Olzscha et al., 2011; Wei et al., 2003) served as a control. Expression of myc-β4, but not myc-α-S824, resulted in aggregation and caused toxicity in neurons (Fig. S5b-c). When each of these proteins was co-transduced into primary neurons together with the mCherry-GFP-LC3 reporter, the total number of fluorescent puncta was not different between myc-β4 and myc-α-S824 neurons (Fig. 5e-f). However, in myc-β4 cells the number of yellow (non-acidic) puncta was increased, while the number of red only (acidic) puncta was decreased (Fig. 5g). These results argue against an overall increase in autophagy induction in the presence of the aggregating protein, but confirm a block in the autophagy flux due to decreased lysosomal acidity.

To further test whether autophagy induction was altered, we monitored the levels of the early autophagy markers Beclin 1 and ATG5 (Yamamoto and Yue, 2014) in HeLa cells transfected with β23-mCherry. These markers were not significantly different in β23-mCherry and mCherry control cells (Fig. 5h-i), suggesting that autophagosome formation was not affected by β proteins. Consistently, early autophagosomes were rarely observed by cryo-ET in either control or β protein-expressing neurons (Supplementary Fig. S4e and Supplementary Table S1). In contrast, real-time PCR revealed that β protein expression induced an upregulation of transcripts of numerous lysosomal proteins (Fig. 5j), a characteristic signature of aberrant lysosomal storage (Sardiello et al., 2009; Settembre et al., 2011). Taken together, our data suggest that β protein aggregates do not affect early stages of autophagy, but impair lysosomal function.

Interactome of β proteins in neurons

To search for the molecular causes of these lysosomal alterations, we characterized the interactome of β proteins in neurons using quantitative label-free mass spectrometry (MS). In these experiments we also used another mCherry-fused artificial amyloid-like protein called β17. The aggregation propensity of the proteins increases from β4 to β17 to β23 (Olzscha et al., 2011; West et al., 1999). Primary cortical neurons lentivirally transduced with β proteins or mCherry were harvested at DIV10+4, a time point when β proteins are still largely soluble and do not cause massive cell death (Supplementary Fig. S1). Immunoprecipitation against mCherry was then performed to isolate interactors, and the total proteome was also analyzed.

Using highly stringent criteria, we identified 30 β4-mCherry interactors, 54 β17-mCherry interactors and 59 β23-mCherry interactors, with an extensive overlap between the three β proteins (Fig. 6a-e and Supplementary Table S2). In addition to confirming interactions found previously in non-neuronal cells (Olzscha et al., 2011), our approach uncovered a number of neuron-specific interactors, including several proteins linked to neurodegenerative disorders, such as Aimp1 (Armstrong et al., 2014), Mark4 (Rovelet-Lecrux et al., 2015) and Ppp2r5d (Louis et al., 2011) (Supplementary Table S2).

Annotation enrichment analysis of the interactors revealed their involvement in key signaling pathways, such as “protein serine/threonine kinase activity”, “GTPase regulator activity”, and “transport” (Supplementary Fig. S6a-c). Another enriched category was “microtubule”, consistent with the impaired morphology of β protein-expressing neurons (Fig. 1e-f). In addition to these general cellular pathways, we found neuron-specific categories, such as “synapse”, “postsynaptic cell membrane” and “neuron projection” (Supplementary Fig. S6a-c). In line with previous proteomic investigations of other aggregates (Hosp et al., 2017; Kim et al., 2016; Olzscha et al., 2011; Woerner et al., 2016), we observed a gradual increase of low-complexity regions in β protein interactomes that paralleled their aggregation propensity (Supplementary Fig. S6d).

Analysis of the total proteome of transduced neurons (which includes the proteins interacting with the aggregates) did not reveal significant changes in the levels of any of the β protein interactors Supplementary Fig. S7a-d, Supplementary Tables S2 and S3). This indicates that their presence in the aggregates was not merely a result of their increased amounts in the cells, nor was their sequestration markedly compensated by increased expression. The unaltered total levels of the interactors, together with their enrichment in the aggregates, suggest that the biologically active cellular pool of these proteins is likely reduced, potentially leading to functional impairments.

AP-3μ1 is sequestered by β protein aggregates, compromising the integrity of the AP-3 complex

The most highly enriched protein in the interactome of all three β proteins was AP-3μ1, the medium subunit of the heterotetrameric AP-3 adaptor complex (Fig. 6b-e). The AP-3 complex is involved in intracellular trafficking of transmembrane proteins, including protein transport to lysosomes (Newell-

Litwa et al., 2007), and the medium subunit is responsible for cargo recognition (Ohno et al., 1998). AP-3µ1 made up 26% of the β4-mCherry-interacting complexes, 17% for β17-mCherry, and 10% for β23-mCherry (Fig. 6f-h), while its amount in the total proteome was not significantly changed (Supplementary Fig. S7b-d). In agreement with our MS data, both β4-mCherry and β23-mCherry co-immunoprecipitated with endogenous AP-3µ1 in neurons (Supplementary Fig. S7e). Immunofluorescence experiments in neuronal cultures showed a high degree of colocalization between co-transfected AP-3µ1 and β proteins (Fig. 6i-j).

To test whether entrapment of AP-3µ1 within the aggregates results in its depletion from the soluble pool, we performed cell fractionation experiments. This showed that AP-3µ1 was reduced in the soluble fraction of β4-mCherry neurons by 30% (Fig. 7a-c). It should be kept in mind that also soluble AP-3µ1 can be partially non-functional due to its aberrant interaction with soluble species of β proteins (Fig. 6b-h and Supplementary Fig. S7e). Taken together, these data suggest that AP-3µ1 can be substantially sequestered by aggregated β proteins. As AP-3µ1 is not highly abundant in neurons (Supplementary Fig. S7f), its sequestration likely results in a partial loss of function.

Defects in single subunits of the AP-3 complex have been previously shown to result in destabilization of the entire complex and premature degradation of its other subunits (Kantheti et al., 1998). We therefore quantified the levels of AP-3δ1, one of the large subunits of the AP-3 complex, in β protein neurons. Although AP-3δ1 was not directly sequestered by β protein aggregates (Supplementary Table S2), its levels were decreased by ~70% (Fig. 7a-b). These results suggest that the partial loss of the medium subunit leads to lower amounts of other AP-3 subunits and likely to a reduction in the levels of intact AP-3 complex in the cell. AP-3 complex deficiency is known to cause defects in biogenesis and function of lysosome-related organelles in mice and in humans, for example in the rare genetic disorder Hermansky-Pudlak syndrome (Dell'Angelica and Bonifacino, 2019). Thus, we hypothesized that AP-3 loss of function may play a role in the lysosomal defects and neurotoxicity caused by β proteins.

AP-3 function is impaired by β proteins, leading to lysosomal defects

To assess the function of the AP-3 complex in the presence of β proteins, we determined the localization of the lysosomal protein Lamp1, a known cargo of AP-3. Lamp1 is at least partially trafficked via the

plasma membrane, and then internalized and transported from the endosomal compartment to the lysosomes in an AP-3 dependent manner (Peden et al., 2004). In conditions of AP-3 deficiency, Lamp1 is recycled from the endosomes back to the plasma membrane, leading to its accumulation at the cell surface (Dell'Angelica et al., 1999; Peden et al., 2002). Immunostaining for surface and total Lamp1 demonstrated significant mislocalization of the protein to the plasma membrane in both β4-mCherry and β23-mCherry neurons (Fig. 7d-e), suggesting that AP-3-dependent transport of lysosomal proteins is impaired. Total Lamp1 levels were not changed in the proteome of β protein expressing neurons (Supplementary Table S3, Supplementary Fig. S7g).

Mice with a homozygous null mutation in AP-3δ1 (mocha mice) exhibit defects in lysosome-related organelles such as melanosomes and platelet dense granules, and show altered secretion of lysosomal enzymes in the kidney, suggesting that AP-3 loss-of-function causes impairments in lysosomes (Swank et al., 1991). We sought to confirm this in a mocha fibroblast cell line, and used functionally rescued mocha cells stably expressing the AP-3δ1 subunit as control (Kent et al., 2012). In agreement with previous reports (Kantheti et al., 1998), the levels of AP-3μ1 were severely reduced in mocha cells (Supplementary Fig. S8a-c), consistent with the instability of the whole complex in the absence of one subunit. When Mocha cells were loaded with LysoTracker Red, we observed reduced numbers of lysosomes per cell (Fig. 7f-g), in line with our findings in LysoTracker-labeled β protein neurons (Fig. 4c). These results confirm that impairment of the AP-3 complex leads to lysosomal defects.

To test whether re-supplying AP-3μ1 would be sufficient to ameliorate β protein toxicity, we quantified cell death in neuronal cultures co-transfected with β proteins and Flag-AP-3μ1 or EGFP as a control. Cleaved Caspase-3 staining demonstrated that co-expression of AP-3μ1 significantly reduced cell death in both β4-mCherry and β23-mCherry cells (Supplementary Fig. S8d-e). Therefore, impaired integrity and function of the AP-3 adaptor complex contributes to β protein toxicity. Altogether, our data strongly suggest that lysosomal defects mediate, at least in part, the toxicity of β protein aggregates in neurons.

Discussion

Here we used rationally designed aggregating proteins to understand the role of the aggregates' gain-of-function toxicity in neurons. It should be kept in mind that β proteins differ from natural amyloids in several aspects. The solvent-exposed and buried face of the rationally designed proteins consist entirely of polar and non-polar amino-acids, respectively, while natural amyloids present a more mixed structure. In addition, natural amyloid fibrils are wider and more resistant to disassembly than those made up of β proteins (Falcon et al., 2018; Fitzpatrick et al., 2017; Olzscha et al., 2011; West et al., 1999; Zhang et al., 2020). Despite these limitations, β proteins have proven very useful in unraveling general mechanisms of aggregate toxicity that apply to natural disease-related proteins (Frottin et al., 2019; Olzscha et al., 2011; Vincenz-Donnelly et al., 2018; Woerner et al., 2016). Apart from fibrillar aggregates, soluble oligomers may also play a role in the effects observed here, as a large fraction of the β proteins remained soluble at the time point of the analyses (Supplementary Fig. S1).

Our integrated structural, functional and molecular approach demonstrates that gain-of-function toxicity of protein aggregates is sufficient to recapitulate crucial cellular aspects of protein misfolding diseases, such as impairment of the autophagy-lysosomal pathway and neurotoxicity. These findings address a long-standing question regarding the role of aggregates as causative agents vs. incidental by-products of disease progression (Arrasate and Finkbeiner, 2012; Haass and Selkoe, 2007), and conclusively show that protein aggregation per se has a deleterious impact on neurons. The toxicity mechanisms triggered by aggregating proteins are multifactorial and involve various cellular processes (Kim et al., 2016; Olzscha et al., 2011). While our results are in agreement with this view, they point to lysosomal degradation as a pathway that is particularly vulnerable in primary neurons.

The lysosomal abnormalities that we observed in β protein neurons are reminiscent of those reported in common neurodegenerative diseases such as Alzheimer's and Parkinson's (Dehay et al., 2012; Suzuki and Terry, 1967; Usenovic et al., 2012). One possible cause of lysosomal defects in protein misfolding disorders is that protein aggregates are targeted by the autophagy-lysosomal pathway (Filimonenko et al., 2010; Hoffmann et al., 2019; Jo et al., 2014; Menzies et al., 2015), but fail to be degraded by lysosomes, accumulating in these organelles and impairing their function (Lamark and

Johansen, 2012). In the case of β proteins, this scenario seems unlikely, since no aggregates were found within lysosomes by cryo-ET or light microscopy.

We propose that impaired trafficking of lysosomal proteins due to an insufficient cellular pool of intact AP-3 complex contributes to the lysosomal defects caused by the aggregates. In agreement with previous studies investigating mutations in other AP-3 subunits (Peden et al., 2002), we show that reduced levels of AP-3μ1 compromise the stability of the whole complex. In turn, AP-3 defects lead to missorting of lysosomal proteins and impair lysosomal function. AP-3 has been implicated in protein trafficking at different subcellular locations, such as direct transport from the Golgi apparatus or internalization from the plasma membrane via the endosomal pathway (Dell'Angelica et al., 1999; Li et al., 2016; Peden et al., 2004). In neurons, the AP-3 complex is also involved in the polarized sorting of proteins to the axonal compartment (Li et al., 2016). Moreover, a number of other proteins related to intracellular transport and to other functions interact with β proteins. Thus, the exact trafficking step(s) impaired by AP-3 deficiency in aggregate-bearing neurons remain to be elucidated. It is also possible that impairment of cellular processes beyond lysosomal trafficking contributes to the deleterious effects of β proteins.

Importantly, previous proteomic studies demonstrated interactions of AP-3μ1 and other subunits of the AP-3 complex with disease-related aggregating proteins including the Arctic mutant of $A\beta_{1-42}$, phosphorylated tau and mutant Huntingtin (Drummond et al., 2020; Hosp et al., 2017; Olzscha et al., 2011; Shirasaki et al., 2012). Sequestration of lysosomal proteins by aggregates and impaired trafficking of lysosomal enzymes was also described in synucleinopathies and in spinal and bulbar muscular atrophy (Chu et al., 2009; Cortes et al., 2014; Decressac et al., 2013; Dehay et al., 2012; Mazzulli et al., 2016). Therefore, compromised intracellular transport of lysosomal components may be an important factor in the pathogenesis of multiple neurodegenerative diseases.

Materials and Methods

Plasmids

For transfection, myc-β4 and myc-β23 (kind gift from Mark Hipp and Ulrich Hartl) were cloned into pmCherry-N1 (Clontech) between KpnI and AgeI restriction sites. pmCherry-N1 was used as control. The mouse AP-3μ1 expression plasmid was purchased from Origene (Ref. MR206629) and consists of AP-3μ1-myc-DDK in pCMV6-ENTRY. For interactome analysis, myc-mCherry, myc-β4-mCherry, myc-β17-mCherry and myc-β23-mCherry were cloned into pENTR1A-164 between restriction sites NotI and EcoRI. For β protein characterization in lentivirally transduced neurons, myc-mCherry and myc-β23-mCherry were cloned between BamHI and XhoI restriction sites of plasmid pFhSynW1, while myc-β4-mCherry was cloned between BamHI and EcoRV. Plasmids for lentiviral expression included the Kozak sequence CCCACC at the 5' terminus of the insert.

Lentivirus production

Hek293T cells for lentiviral packaging were purchased (Lenti-X 293T cell line, Takara) and expanded to 70-85% confluency in DMEM Glutamax (+ 4.5g/L D-Glucose, - Pyruvate) supplemented with 10% FBS (Sigma), 1% G418 (Gibco), 1% NEAA (Thermo Fisher), 1% Hepes (Biomol). Only low passage cells were used. For lentiviral production, three T75cm^2 flasks (Falcon) containing 5.7 million cells each were seeded and henceforth cultured in medium without G418. On the following day, cells were transfected with the expression plasmid pFhSynW2, and the packaging plasmids psPAX2 and pVsVg (all three kindly provided by Prof. Dieter Edbauer) using TransIT-Lenti transfection reagent (Mirus). The transfection mix was incubated for 20 min at room temperature (RT) and in the meanwhile, cell medium was exchanged. 1 ml transfection mix was added to each flask and left overnight. The medium was exchanged on the next day. After 48-52 h, culture medium containing the viral particles was collected and centrifuged for 10 min at 1200 x g. Then, the supernatant was filtered through 0.45 μm pore size filters using 50 ml syringes, transferred to Ultra-clear centrifuge tubes (Beckman), and centrifuged at 100,000 x g for 2 h with in the Avanti JXN-30 centrifuge, rotor JS-24.38 (Beckman). Supernatant was discarded and the lentivirus pellet resuspended in TBS-5 buffer (50 mM Tris-HCl, pH 7.8, 130 mM NaCl, 10 mM KCl, 5 mM $MgCl_2$). After aliquoting, virus was stored at -80°C. For interactome analyses, lentivirus was produced using the pLV-Syn vector (derived from pLenti7.3-V5-Dest) and the packaging vectors pCMVdelta8.91 and pMD2_G (kindly provided by Dr. Alexandra Lepier).

Preparation of EM grids

R 2/1 Holey Carbon Au 200 mesh EM grids (Quantifoil) were coated with approximately 20 nm of carbon in a MED 020 carbon coater (BAL-TEC) and made hydrophilic for 45 s in a PDC-3XG plasma cleaner (Harrick). For HeLa cell culture, the grids were UV-sterilized in a Herasafe HR18 cell culture hood (Heraeus) for 30 min. For neuronal cultures, the grids were sterilized in ethanol for 10 min, washed several times in double-distilled water and transferred to culture dishes containing water. Grids and dishes for neuronal cultures were coated with poly-D-lysine (Sigma-Aldrich; 1 mg/ml in borate buffer) for 24 h and washed three times with water. Subsequently, the grids were coated with laminin (Thermo Fisher; 5.0 µg/ml in PBS) for 24 h, washed with PBS three times and placed in Neurobasal medium supplemented with B27 containing 0.5 mM Glutamine (all reagents from Thermo Fisher). During washes and medium exchange steps, grids were transferred into another dish containing the appropriate liquid to prevent them from drying.

Primary neuron culture

Primary neurons were prepared from E14.5-15.5 CD-1 or C57BL/6 wildtype embryos. Pregnant mice were sacrificed by cervical dislocation, the uterus was removed from the abdominal cavity and placed into a 10 cm sterile Petri dish on ice containing dissection medium, consisting of Hanks' balanced salt solution (HBSS) supplemented with 0.01 M HEPES, 0.01 M MgSO4, and 1% Penicillin / Streptomycin. Each embryo was isolated, heads were quickly cut, brains were removed from the skull and immersed in ice-cold dissection medium. Subsequently, cortical hemispheres were dissected and meninges were removed under a stereo-microscope. For each sample, cortical or hippocampal tissue from typically six to seven embryos was transferred to a 15 ml sterile tube and digested with 0.25% trypsin containing 1 mM 2,2′,2″,2‴-(ethane-1,2-diyldinitrilo) tetraacetic acid (EDTA) and 15 µl 0.1% DNAse I for 20 minutes at 37°C. The enzymatic digestion was stopped by removing the supernatant and washing the tissue twice with Neurobasal medium (Invitrogen) containing 5% FBS. The tissue was resuspended in 2 ml medium and triturated to achieve a single-cell suspension. Cells were spun at 130-180 x g, the supernatant was removed, and the cell pellet was resuspended in Neurobasal medium with 2% B27 (Invitrogen), 1% L-Glutamin (Invitrogen) and 1% Penicillin/Streptomycin (Invitrogen). For cryo-ET, Neurons were plated on the coated grids within 24-well plates (60,000 per well). For MS analysis,

cells were cultured on 6 well-plates (Thermo Fisher Scientific) (500,000 neurons per well) coated with 1 mg/ml Poly-D-Lysine (Sigma) and 1 µg/ml Laminin (Thermo Fisher Scientific). For immunostaining, neurons were cultured on 13 mm coverslips, coated as above, in 24 well-plates (Thermo Fisher Scientific). For MTT assay, neurons were cultured in coated 96 well-plates. Transfection was performed using Calcium Phosphate according to the protocol from (Jiang and Chen, 2006) or using Lipofectamine2000 (Thermo Fisher Scientific) according to the manufacturer's protocol. For lentiviral transduction, viruses were thawed and immediately added to freshly prepared neuronal culture medium. A fifth of the medium from cultured neurons was removed and the equivalent volume of virus-containing medium was added. Typically, 1 µl/cm^2 of virus was added, but this amount was sometimes adjusted to match protein expression levels among different constructs.

HeLa cell culture

HeLa CCL-2 (ATCC) cells were grown in DMEM medium (Life Technologies) with 10% FBS (Life Technologies), 0.5 mM L-Glutamine (Life Technologies), 1% MEM NEAA 100x (Life Technologies), 1% Penicillin/Streptomycin (10,000 U/mL; Life Technologies) at 37°C and 5% CO2. HeLa cells were transfected using FuGENE 6 transfection reagent (Promega) according to the manufacturer's instructions. For cryo-ET, approximately 25,000 cells were seeded in 35 mm culture dishes (BD Falcon) containing four pre-treated EM grids 24 h prior to transfection. For western blot experiments, cells were plated in 6 cm dishes 24 h prior to transfection (250,000 cells/well). To inhibit autophagy, cells were treated with 50 µM chloroquine in water (Sigma). HeLa cells were harvested 24-48 h after transfection.

Mocha cell culture

Mocha cells and control cells stably expressing AP-3δ1 (AP-3δ1+ cells) were kind gift of Andrew A. Peden. Cells were cultured in DMEM supplemented with 10% FCS and 1% penicillin/streptomycin. For AP-3δ1+ cells, 0.2mg/ml hygromycin B was added to the medium. For lysosome counting, 100,000 cells were seeded onto glass coverslips. Cells were treated with 150 nM LysoTracker Red (Thermo Fisher) for 30 min one day after seeding, washed with PBS and fixed with 4% PFA. Lysosomes were automatically quantified using a custom-made CellProfiler pipeline. For Western Blot, 250,000 cells were seeded in 6-well plates and harvested one day after seeding.

Immunostaining

Cells were fixed with 4% paraformaldehyde in PBS for 20 min; remaining free groups of PFA were blocked with 50 mM Ammonium chloride in PBS for 10 min at RT. Cells were rinsed once with PBS and permeabilized with 0.25% Triton X-100 in PBS for 5 min. After permeabilization, cells were washed with PBS and blocked with 2% BSA (w/v) (Roth) and 4% donkey serum (v/v) (Jackson Immunoresearch Laboratories) in PBS for 30 min at RT. Coverslips were transferred to a light-protected humid chamber and incubated in primary antibody diluted in blocking solution for 1 h. The following primary antibodies were used: anti-mCherry (AB0040-200, Origene, 1:500), anti-myc 9E10 (13-2500, Thermo Fisher, 1:100), anti-cleaved Caspase-3 (9661S, CST, 1:500) and anti-Flag (TA-50011-100; Origene, 1:500). Cells were washed with PBS and incubated with secondary antibodies (Jackson Immunoresearch Laboratories) diluted 1:250 in blocking solution, with 0.5 µg/ml DAPI added to stain the nuclei. Coverslips were mounted on Menzer glass slides using Dako or Prolong Glass fluorescence mounting medium (Thermo Fisher). Confocal images were obtained at a spinning disc microscope (Zeiss) or SP8 confocal microscope (Leica).

Colocalization analysis for β-mCherry proteins and AP-3µ1 was performed on single plane images of double-transfected neurons. A ROI was manually drawn around the soma of each cell in the mCherry channel and the ImageJ plug-in Coloc 2 was used to calculate the Pearson's correlation coefficient.

Lamp1 staining

Transduced cortical and hippocampal neurons were used. Stainings were performed at DIV 10+4 and 10+5 (three cultures for each time-point) as described (Glynn and McAllister, 2006). Briefly, live neurons cultured on coverslips were washed with ice-cold PBS and placed in a pre-cooled humid dark chamber that was kept on ice. Primary antibody (rat α-Lamp1, Abcam, Reference ab25245) diluted 1:300 in blocking solution was added for 1 h. After washing with ice-cold PBS, secondary antibody (donkey α-rat 488) diluted 1:250 was added for 30 min. Cells were washed with ice-cold PBS and fixed with ice-cold 4% PFA in PBS for 10 min at RT. Next steps were performed as described above in Immunostaining, using the same primary antibody, but changing the secondary to donkey α-rat 647 to differentiate between surface and total Lamp1.

Colocalization analysis was performed on maximum intensity projection images of transduced neurons. A ROI was manually drawn around the soma of each cell in the mCherry channel. A background

subtraction of rolling ball radius of 50 pixels was performed in all images. The ImageJ plug-in Coloc 2 was used to calculate the Pearson's correlation coefficient between surface and total Lamp1.

Neuronal viability measurements and Sholl analysis

For transduced neurons, viability was determined with the MTT assay using Thiazolyl Blue Tetrazolium Bromide (MTT) reagent purchased from Sigma-Aldrich. Neurons were cultured in 96-well plates. First, cell medium was exchanged for 100 µl of fresh medium. Then, 20 µl of 5 mg/ml MTT in PBS was added and incubated for 2-4 h at 37°C, 5% CO_2. Subsequently, 100 µl solubilizer solution (10% SDS, 45% Dimethylformamide in water, pH 4.5) was added, and on the following day absorbance was measured at 570 nm. Each condition was measured in triplicates and absorbance values averaged for each experiment.

For transfected neurons, toxicity was quantified by an investigator blinded to the conditions based on immunostaining for cleaved caspase-3.

For Sholl analysis, mCherry channel was used to visualize neuronal morphology. Coverslips were immunostained against mCherry and imaged with a 40x objective. Maximum intensity projections were analyzed. First, cell morphologies were semiautomatically traced with the Simple Neurite Tracer plug-in of ImageJ in a blinded way. Then, complexity of the traced neurons was quantified with the Sholl analysis plug-in of ImageJ using a custom-made macro for batch processing.

Live cell light microscopy

Samples were imaged using brightfield and epifluorescence widefield microscopy in a CorrSight microscope (FEI) using FEI MAPS 2.1 software. Low magnification overview images were acquired with a 5x air objective (Plan-ApoChromat, NA 0.16; Carl Zeiss). For high magnification image stacks, a 63x oil immersion objective (Plan Achromat, NA 1.4; Carl Zeiss) was used. Cells were kept on a 37 °C heated stage in a homemade climate chamber infused with humidified air and 5% CO_2 gas. Cells were located at low magnification and z-stacks were acquired in 500 nm steps over the whole cell height at high magnification.

For the analysis of lysosome size and number, neuronal cultures expressing β23-mCherry, β4-mCherry or mCherry were incubated with 75 nM LysoTracker Green DND-26 (Thermo Fisher Scientific) for 30 min according to manufacturer's instructions. The mCherry signal was used to assess the cell perimeter

and only lysosomes within that perimeter were measured. The mCherry signal of each cell was isolated by automatic thresholding using a homemade script written for Fiji software (Schindelin et al., 2012). The size of each lysosome was manually measured in its in-focus plane using Fiji software. The Pearson correlation coefficient was measured using JACoP plugin in Fiji software (Bolte and Cordelieres, 2006).

For autophagy flux analysis with mCherry-GFP-LC3 reporter, primary cortical neurons were seeded in imaging plates with a glass-bottom (Nunc) and co-transfected at DIV 10 with the mCherry-GFP-LC3 reporter (gift from Anne Brunet, Addgene plasmid # 110060) and either α-S824 or myc-β4 protein. Life-imaging was performed at DIV 10+3 using a Spinning Disc Microscope SN 3834000224 (Zeiss) and the Visiview Software (Visitron Systems). Single imaging planes of each neuron were selected for autolysosome and autophagosome quantification. The total number of puncta and the number of yellow puncta were manually quantified for each neuron. The number of red puncta was calculated by subtracting the number of yellow puncta from the total. All quantifications were performed in a blinded fashion to the analyzed condition.

Sample vitrification

Cells were vitrified using a home-made manual gravity-driven plunge-freezer. Before plunge-freezing, cells were treated with 10% glycerol (Sigma-Aldrich) in medium as a cryoprotectant for 1 – 5 min. In addition, in some cases cells were stained with 3% Annexin V, Alexa Fluor 488 conjugate (Life Technologies) 15 minutes prior to vitrification to identify dead cells. During plunge-freezing, EM grids were blotted for 8 s with filter paper No. 1 (Whatman) from the back side and immediately frozen in liquid ethane/propane (37% / 63%; Linde) kept at liquid nitrogen temperature. Grids were transferred to liquid nitrogen and excess ethane/propane was blotted with pre-cooled filter paper. Grids were stored in liquid nitrogen until further use.

Cryo-light microscopy

Frozen grids were fixed into FIB C-clip rings to increase mechanical stability. Samples were transferred to a CorrSight shuttle (FEI) and mounted on the CorrSight cryo-stage (FEI) maintained at liquid nitrogen temperature for cryo-light microscopy. Samples were imaged using widefield or spinning-disk confocal, epifluorescence microscopy using FEI MAPS 2.1 software. Images were acquired with a 1344 x 1024

pixel camera (pixel size 6.4 µm, Hamamatsu Digital Camera C10600 ORCA-R2). Grids were imaged in widefield mode at low magnification with a 5x air objective (Plan-ApoChromat, NA 0.16; Carl Zeiss) and in spinning-disk confocal mode at high magnification with a 40x air objective (EC Plan-Neofluar, NA 0.9; Carl Zeiss) for identification of cells and/or aggregates. Image acquisition and further SEM correlation was performed by three-point correlation using FEI MAPS 2.1 software.

Cryo FIB SEM

Grids imaged by light microscopy were mounted on a transfer shuttle designed for a cryo-loading system (Rigort et al., 2010) and loaded into a Quanta 3D FEG dual-beam FIB/SEM (FEI). Grids were sputtered with platinum (10 mA, 30 s) in a PP3000T loading system (Quorum) to reduce charging effects during electron imaging. Grids were loaded into the FIB chamber and coated with organometallic platinum as a protective layer for ion beam milling. Grids were imaged with the scanning electron beam operated at 5 kV / 12 pA and regions of interest (ROI) were identified via cryo-LM/SEM 3-point correlation using MAPS 2.1 software. ROIs were thinned down at tilt angles of 18° - 20° with the focused ion beam operated at 30 kV. The beam currents where set to 1 nA at approximately 1 µm distance from the ROI, 500 pA at 750 nm, 300 pA at 400 nm, 100 pA at 250 nm, 50 pA at 100 nm and 30 pA at 75 nm for polishing. Grids were sputtered once more with platinum (10 mA, 5 s) after milling to increase conductivity of the lamellae for VPP imaging.

Cryo ET

Cryo-TEM was performed on a Titan Krios cryo-TEM (FEI) operated at 300 kV, equipped with a FEG, post-column energy filter (Gatan) and Volta phase plate (Danev et al., 2014). Tomograms were acquired on a K2 Summit direct electron detector (Gatan) in dose fractionation mode (0.08 frames per second) using SerialEM (Mastronarde, 2005). Lamella overview images were acquired at 3600x magnification (pixel size: 38.93 Å) and stitched using the automatic photo merge in Adobe Photoshop. For cryo-LM – cryo-TEM correlation, stitched lamella TEM overview images were imported into MAPS and aligned with cryo-LM data. Tilt series were recorded at -0.5 µm defocus for VPP imaging at 33000x magnification (pixel size: 4.21 Å), with an angular increment of 2° and typically ranged from -50° to 60°. The total dose was restricted to approximately 120 electrons / Å² per tomogram.

Tomogram reconstruction and data processing

K2 frames were aligned and combined using an in-house software based on previous work (Li et al., 2013). Tilt-series were aligned using patch tracking from the IMOD software package (Kremer et al., 1996) and reconstructed by weighted back projection. The platinum layer for VPP imaging and large pieces of surface ice contamination were computationally removed to increase signal-to-noise ratio (Fernandez et al., 2016). The resulting tilt-series were realigned and reconstructed again. Tomograms were binned four times to a final pixel size of 16.84 Å to increase contrast.

Tomogram segmentation was performed using Amira (FEI). Membranes and microtubules were automatically segmented using TomoSegMemTV (Martinez-Sanchez et al., 2014) and corrected using Amira. β-protein fibrils were traced on denoised tomograms (non-local means filter) by removing membranes and macromolecules followed by density thresholding and subsequent skeletonization. For the identification of ribosome positions, template matching was applied using the pyTOM toolbox in MATLAB (Mathworks) as previously reported (Hrabe et al., 2012). A human 80S ribosome structure (PDB: 4UG0) (Khatter et al., 2015) was filtered to 40 Å and used as a template. Coordinates of ribosomes identified via template matching were imported into Amira and masked with the filtered molecular structure.

Western Blotting

Cells were lysed in 50 mM Tris-HCl, pH 7.4, 150 mM NaCl, 2 mM EDTA, 1% Triton X-100 with protease and phosphatase inhibitor tablets (Roche). Lysates were centrifuged for 10 min at 4,000 x g (neurons) or 14,000 x g (HeLa) and 4°C and supernatants collected (soluble fraction). Pellets were used as insoluble fraction, whole extracts were used as total. Proteins were separated on 12% or 15 % SDS-PAGE gels and transferred onto PVDF membranes using a Trans-Blot Turbo transfer system (Bio-Rad). Blocking was performed with 3% BSA, 5% dried milk (Roth) in TBS-T for 1 h at RT. Primary antibodies were diluted 1:1000 in 3% BSA in TBS-T, 0.01% Sodium azide and incubated for 2 days at 4°C. Secondary antibodies were diluted 1:5000 in 5% dried milk in TBS-T and applied for 2 h at RT. Tubulin-Rhodamine (Bio-Rad) was diluted 1:2500 and added together with the secondary antibodies. Detection was performed using the Chemidoc MP imaging system (Bio-Rad). Primary antibodies used were anti-LC3B (D11) (3868, Cell Signaling), anti-p62 (ab56416, Abcam), anti-GFP (632381, Clontech), hFAB rhodamine anti-tubulin (12004166, Bio-Rad), anti-myc 9E10 (13-2500, Thermo Fisher), anti-Atg5

(D5F5U, Cell Signaling), anti-beclin-1 (3495, Cell Signaling), anti-HPRT (ab10479, Abcam), anti-AP-3μ1 (ab201227, Abcam), anti-AP-3δ1 (kind gift from Andrew A. Peden) and anti-tubulin (T9026, Sigma). For fluorescent Western Blots, secondary antibodies were: StarBright Blue 520 Goat Anti-Mouse, StarBright Blue 520 Goat Anti-Rabbit, StarBright Blue 700 Goat Anti-Mouse, StarBright Blue 700 Goat Anti-Rabbit. Band density quantification was performed with ImageJ and normalized to loading controls.

Quantitative RT-PCR

RNA isolation and purification was performed using a Crystal RNA mini Kit (Biolab) according to the manufacturer's instructions. RNA quantification and quality control were done with a Nanodrop spectrophotometer (PeqLab). cDNA was synthesized using a High-Capacity cDNA Reverse Transcription Kit (Applied Biosystems) according to the manufacturer's instructions. cDNA was diluted 1:50, each 8 µl reaction contained 4 µl diluted cDNA, 0.2 µl dilutions of each primer (25 µM stock), and 3.6 µl Luna Universal Probe qPCR Master Mix (New England BioLabs). The primers were described previously (Fernandez-Mosquera et al., 2017).

Immunoprecipitation

For AP-3μ1 immunoprecipitation, lysates of transduced cortical neurons cultured in 6-well plates were were incubated overnight with 2 µl of rabbit α-AP-3μ1 antibody (Abcam, Reference ab201227) on a rotating wheel at 4°C. 50 µl of Protein G Sepharose 4 Fast Flow (Sigma) slurry were washed, resuspended in lysis buffer (50 mM Tris-HCl, pH 7.4, 150 mM NaCl, 2 mM EDTA, 1% Triton X-100 with protease and phosphatase inhibitor tablets (Roche)), and added to the lysates. The mix was incubated for 2 h at RT on a rotating wheel. Further steps were performed as described by the manufacturer, but performing all washes with lysis buffer.

For interactome analysis, cortical neurons (500.000 cells/condition) were harvested in ice-cold lysis buffer (0,25% NP40, 5% glycerol, 50 mM Tris HCl, 150 mM NaCl) containing protease inhibitor (Roche), DNAse (5 µl/ml) and RNAse (0,5 µl/ml). Thermo Scientific™ Pierce™ Protein G Agarose (10 µl/100 µg IgG) was used for purification and immunoprecipitation of IgG antibodies. Serum samples containing IgG were incubated with Protein G agarose in a buffer that facilitates binding (20 mM sodium phosphate) for 1 h. Then, neuronal lysates were loaded onto IgG-protein G Agarose and incubated for 4 h. Non-IgG and non-antigen components were discarded from the sample by washing with 0,1% NP40, 5%

Glycerol, 50 mM Tris HCl, 150 mM NaCl. Enriched proteins were next isolated and processed in a step-wise manner. First, proteins were denatured, digested and cysteines reduced for 1 hour at 20°C by adding 8 M Urea, 40 mM Hepes pH 8.0, 1 µg LysC and 10 mM DTT. Next, urea concentration was lowered to 2 M by adding 50 mM ammonium bicarbonate in MilliQ water. Trypsin (1 µg) was added to the protein-peptide mix and samples were subjected to 55 mM chloroacetamide for 1 h to alkylate cysteine residues. Alkylation was quenched by adding 2 M urea / 50 mM thiourea and overnight digestion was carried out after addition of 1 µg fresh trypsin. Interactome analysis was conducted in four independent biological replicates.

Complete neuronal proteome precipitation

Complete neuronal proteomes where extracted as described previously (Hornburg et al., 2014). In brief, cells were lysed in lysis buffer (4% SDS, 10 mM Hepes, pH 8.0) and reduced with 10 mM DTT for 30 min. The proteins were then subjected to 45 min of alkylation with 55 mM iodoacetamide. Acetone precipitation was performed to remove the SDS: Acetone (-20 °C) was added to 100 µg of proteins to a final concentration of 80% v/v, and proteins were precipitated overnight at -20 °C. The supernatant was removed after 15 min of centrifugation (4 °C, 16,000 x g) followed by washing with 80% acetone (-20 °C). Residual acetone was evaporated at 20°C. The protein pellet was dissolved in 50 µl of 6 M urea/2 M thiourea, 10 mM Hepes, pH 8.0. LysC (1 µg) digestion was carried out for 2 h at 20°C. The samples were incubated with 1 µg trypsin for overnight digestion, and peptides were desalted on C18 solid phase extraction.

Solid phase extraction

Stage Tips were prepared with 3xC18 material for rapid desalting and step elution of the peptide mixtures. Stage Tips were rinsed with MeOH and Buffer A (0.5% acetic acid). Samples were added to the staging tips and washed with buffer A. Buffer B (80% Acetonitrile, 0.5% acetic acid) was used to elute the samples. Speedvac was used to remove the solvent from the samples. The samples were then resuspended in 10 µl buffer A* (0.5% AcOH, 0.1% TFA, 2% ACN).

LC-MS/MS

Peptides were separated on EASY-nLC 1000 HPLC system (Thermo Fisher Scientific, Odense, Denmark). Columns (75-µm inner diameter, 40-cm length) were in-house packed with 1.9-µm C18 particles (Dr. Maisch GmbH, Ammerbuch-Entringen, Germany). Peptides were loaded in buffer A (0.5% formic acid) and separated with a gradient from 7% to 60% buffer B (80% acetonitrile, 0.5% formic acid) within 3.5 h at 200 nl/min. The column temperature was set to 60 °C. A quadrupole Orbitrap mass spectrometer (Q Exactive, Thermo Fisher Scientific) was directly coupled to the liquid chromatograph via a nano-electrospray source. The Q Exactive was operated in a data-dependent mode. The survey scan range was set to 300 to 1,650 m/z, with a resolution of 70,000 at m/z 200. Up to 15 most abundant isotope patterns with a charge of >= 2 were subjected to Higher-energy collisional dissociation (Olsen et al., 2007) with a normalized collision energy of 25, an isolation window of 2 Th, and a resolution of 17,500 at m/z 200. To limit repeated sequencing, dynamic exclusion of sequenced peptides was set to 30 s. Thresholds for ion injection time and ion target value were set to 20 ms and 3 × 10E6 for the survey scans and to 60 ms and 10E6 for the MS/MS scans. Data were acquired using Xcalibur software (Thermo Scientific).

MS data analysis

To process MS raw files, we employed MaxQuant software (v. 1.5.7.10) (Cox & Mann, 2008). Andromeda (Cox et al., 2011), which is integrated into MaxQuant, was used to search MS/MS spectra against the UniProtKB FASTA database. For the standard immunoprecipitation and pre-loaded serum, enzyme specificity was set to trypsin and LysC. For all the experiments, N-terminal cleavage to proline and up to two miscleavages were allowed. Peptides with a minimum length of seven amino acids were considered for identification. Oxidation, acetylation and deamidation were set as variable modifications (maximum number of modifications per peptide was 5). A false discovery rate (FDR) cut-off of 1% was applied at the peptide and protein levels. Initial precursor mass deviation of up to 4.5 ppm and fragment mass deviation up to 20 ppm were allowed. Precursor ion mass accuracy was improved by time-dependent recalibration algorithms in MaxQuant. The cut-off score (delta score) for accepting individual MS/MS spectra was 17.

The proteome fasta file from *Mus musculus* (Taxon identifier: 10090) was used as a library for matches. Nonlinear retention time alignment (Cox and Mann, 2008; Cox et al., 2011) of all measured samples was performed in MaxQuant. “Match between runs,” which allows the transfer of peptide identifications

in the absence of sequencing, was enabled with a maximum retention time window of 0.7 min. Furthermore, we filtered our data by requiring a minimum peptide ratio count of 1 in MaxLFQ. Protein identification required at least one razor peptide (Cox and Mann, 2008). Proteins that could not be discriminated on the basis of unique peptides were grouped into protein groups. Co-immunoprecipitated proteins were considered interactors if they were significantly enriched compared to the control samples applying a 5% permutation-based FDR cut-off (see below).

For statistical and bioinformatic analysis, as well as for visualization, we used the open Perseus environment, which is part of MaxQuant. The numerical data was transformed to log2(x). Proteins were filtered for common contaminants; proteins identified only by site modification and reverse proteins were excluded. Missing values in pairwise comparisons were imputed with a normal distribution (width = 0.3 x standard deviation; down shift = 1.8 x standard deviation) was performed in Perseus. Proteins were only considered if they were detected with at least three valid values among quadruplicates in at least one condition. For pairwise comparison of proteomes and determination of significant differences in protein abundances, t-test statistics were applied with a permutation-based FDR of 5% and S0 of 1. The resulting significant outliers for each of the sample pairs were analyzed for gene ontology (GOCC) (Harris et al., 2004), biological ontology (GOBP), Molecular function (GOMF), protein complexes (CORUM) (Ruepp et al., 2010), and protein families and domains (Pfam) (Finn et al., 2014) annotation enrichments. The data was displayed in a scatter plot for visual representation. For protein abundance ranking, summed peptide intensities from MaxQuant (median of at least 3 valid values within quadruplicates) were divided by the molecular weight to adjust for protein size bias and estimate the abundance rank of each protein within the proteome. Log10 corrected intensities were plotted against the rank.

To calculate the content of disordered regions, we employed R (rjson and seqinr libraries). First, amino acids that are predicted with low complexity long region (IUPred-L) were mapped to sequences of proteins that are significant outliers in either of the β protein interactomes as well as for the entire population of proteins identified in the interactomes. Next, the ratio of all amino acids and those predicted with low complexity was calculated. To determine the significance of differences between the individual populations, a two-sample Wilcoxon test was performed on the ratio distributions.

Aggregate composition estimation

To estimate the relative mass composition of the protein aggregates, the median of log2 MaxLFQ intensity (requiring at least 2 valid values) was calculated across quadruplicates for the β protein samples and the mCherry controls, respectively. Missing values in the mCherry samples were imputed with a normal distribution on the log2 scale (width = 0.3 x standard deviation; down shift = 1.8 x standard deviation). Next, the non-log (median) intensity of each protein in the β protein samples was subtracted by the respective non-log intensity derived from the mCherry samples. This transformation corrects for the overall background signal in the immunoprecipitation. The resulting intensities roughly correspond to the relative abundance in the aggregate (= composition) and are plotted as fractions in pie charts. Note that we did not apply an FDR or p-value cut-off for this analysis. By subtracting protein intensity of the mCherry controls from those in the β protein samples, small differences (which associate with larger p-values and FDRs) have a diminishing contribution to the overall aggregate composition estimate. In the pie charts, proteins with at least 3% intensity contribution are listed.

Statistical analysis

Statistical analysis of the MS data is described in the previous section. Statistical analysis of other data was performed using Origin Pro 2015G or GraphPad Prism 6. Data are presented as means ± standard deviation unless indicated otherwise.

Acknowledgements

We thank F. Ulrich Hartl, Mark S. Hipp, Massimiliano Stagi, Georg H. H. Borner and Shivani Tiwary for helpful discussions; Günter Pfeifer, Jürgen Plitzko and Miroslava Schaffer for electron microscopy support; Qiang Guo for ribosome template matching; Andrew A. Peden, F. Ulrich Hartl and Mark S. Hipp sharing cell lines, antibodies and plasmids; Alexandra Lepier, Dieter Edbauer and Carina Lehmer for lentiviral plasmids and generous help with lentivirus generation; Martin Dodel for excellent technical assistance; and Daniel del Toro Ruiz for kind help with image analysis. This work was funded by the European Research Council (ERC) Synergy Grant under FP7 GA number ERC-2012-*SyG_318987*-Toxic Protein Aggregation in Neurodegeneration (ToPAG) (to M.M., W.B. and R.K.); ERC Starting Grant MitoPexLysoNETWORK 337327 (to N.R.); Deutsche Forschungsgemeinschaft (DFG, German Research Foundation) through Germany's Excellence Strategy - EXC 2067/1- 390729940 (to R.F.-B.); and by the Max Planck Society for the Advancement of Science.

Author contributions

I.R.-T. performed most of the cell biology assays and prepared neurons for proteomic analysis. T.S. performed cryo-ET and LysoTracker experiments in neurons. D.H. performed proteomic analysis. A.M. quantified cell death in neurons co-expressing β proteins and AP-3μ1, and prepared neurons for cryo-ET and LysoTracker experiments in neurons. L.F.-M. and N.R. performed Western blots and RT-PCR for autophagy-lysosomal markers. D.F. and P.A. assisted with immunostaining and biochemistry, respectively. I.R.-T., T.S., D.H. and I.D. prepared the figures. M.M., W.B., R.K., F.M., N.R., R.F.-B. and I.D. designed research. F.M., R.F.-B. and I.D. supervised research. R.F.-B. and I.D. wrote the paper with input from the other authors.

Conflict of interest

The authors declare no competing interests.

References

Abeliovich, A., and A.D. Gitler. 2016. Defects in trafficking bridge Parkinson's disease pathology and genetics. *Nature*. 539:207-216.

Abraham, R., R. Hendy, and P. Grasso. 1968. Formation of myeloid bodies in rat liver lysosomes after chloroquine administration. *Exp Mol Pathol*. 9:212-229.

Armstrong, L., R. Biancheri, C. Shyr, A. Rossi, G. Sinclair, C.J. Ross, M. Tarailo-Graovac, W.W. Wasserman, and C.D. van Karnebeek. 2014. AIMP1 deficiency presents as a cortical neurodegenerative disease with infantile onset. *Neurogenetics*. 15:157-159.

Arrasate, M., and S. Finkbeiner. 2012. Protein aggregates in Huntington's disease. *Exp Neurol*. 238:1-11.

Bauerlein, F.J.B., I. Saha, A. Mishra, M. Kalemanov, A. Martinez-Sanchez, R. Klein, I. Dudanova, M.S. Hipp, F.U. Hartl, W. Baumeister, and R. Fernandez-Busnadiego. 2017. In Situ Architecture and Cellular Interactions of PolyQ Inclusions. *Cell*. 171:179-187 e110.

Bolte, S., and F.P. Cordelieres. 2006. A guided tour into subcellular colocalization analysis in light microscopy. *J Microsc*. 224:213-232.

Brothers, H.M., M.L. Gosztyla, and S.R. Robinson. 2018. The Physiological Roles of Amyloid-beta Peptide Hint at New Ways to Treat Alzheimer's Disease. *Front Aging Neurosci*. 10:118.

Chiti, F., and C.M. Dobson. 2017. Protein Misfolding, Amyloid Formation, and Human Disease: A Summary of Progress Over the Last Decade. *Annu Rev Biochem*. 86:27-68.

Chu, Y., H. Dodiya, P. Aebischer, C.W. Olanow, and J.H. Kordower. 2009. Alterations in lysosomal and proteasomal markers in Parkinson's disease: relationship to alpha-synuclein inclusions. *Neurobiol Dis*. 35:385-398.

Cortes, C.J., H.C. Miranda, H. Frankowski, Y. Batlevi, J.E. Young, A. Le, N. Ivanov, B.L. Sopher, C. Carromeu, A.R. Muotri, G.A. Garden, and A.R. La Spada. 2014. Polyglutamine-expanded androgen receptor interferes with TFEB to elicit autophagy defects in SBMA. *Nature neuroscience*. 17:1180-1189.

Cox, J., and M. Mann. 2008. MaxQuant enables high peptide identification rates, individualized p.p.b.-range mass accuracies and proteome-wide protein quantification. *Nat Biotechnol*. 26:1367-1372.

Cox, J., N. Neuhauser, A. Michalski, R.A. Scheltema, J.V. Olsen, and M. Mann. 2011. Andromeda: a peptide search engine integrated into the MaxQuant environment. *J Proteome Res*. 10:1794-1805.

Cuervo, A.M., L. Stefanis, R. Fredenburg, P.T. Lansbury, and D. Sulzer. 2004. Impaired degradation of mutant alpha-synuclein by chaperone-mediated autophagy. *Science*. 305:1292-1295.

Danev, R., B. Buijsse, M. Khoshouei, J.M. Plitzko, and W. Baumeister. 2014. Volta potential phase plate for in-focus phase contrast transmission electron microscopy. *Proc Natl Acad Sci U S A*. 111:15635-15640.

Decressac, M., B. Mattsson, P. Weikop, M. Lundblad, J. Jakobsson, and A. Bjorklund. 2013. TFEB-mediated autophagy rescues midbrain dopamine neurons from alpha-synuclein toxicity. *Proc Natl Acad Sci U S A*. 110:E1817-1826.

Dehay, B., A. Ramirez, M. Martinez-Vicente, C. Perier, M.H. Canron, E. Doudnikoff, A. Vital, M. Vila, C. Klein, and E. Bezard. 2012. Loss of P-type ATPase ATP13A2/PARK9 function induces general lysosomal deficiency and leads to Parkinson disease neurodegeneration. *Proc Natl Acad Sci U S A*. 109:9611-9616.

Dell'Angelica, E.C., and J.S. Bonifacino. 2019. Coatopathies: Genetic Disorders of Protein Coats. *Annu Rev Cell Dev Biol*. 35:131-168.

Dell'Angelica, E.C., V. Shotelersuk, R.C. Aguilar, W.A. Gahl, and J.S. Bonifacino. 1999. Altered trafficking of lysosomal proteins in Hermansky-Pudlak syndrome due to mutations in the beta 3A subunit of the AP-3 adaptor. *Mol Cell*. 3:11-21.

Drummond, E., G. Pires, C. MacMurray, M. Askenazi, S. Nayak, M. Bourdon, J. Safar, B. Ueberheide, and T. Wisniewski. 2020. Phosphorylated tau interactome in the human Alzheimer's disease brain. *Brain*. 143:2803-2817.

Falcon, B., W. Zhang, A.G. Murzin, G. Murshudov, H.J. Garringer, R. Vidal, R.A. Crowther, B. Ghetti, S.H.W. Scheres, and M. Goedert. 2018. Structures of filaments from Pick's disease reveal a novel tau protein fold. *Nature*. 561:137-140.

Fernandez, J.J., U. Laugks, M. Schaffer, F.J. Bauerlein, M. Khoshouei, W. Baumeister, and V. Lucic. 2016. Removing Contamination-Induced Reconstruction Artifacts from Cryo-electron Tomograms. *Biophys J*. 110:850-859.

Fernandez-Mosquera, L., C.V. Diogo, K.F. Yambire, G.L. Santos, M. Luna Sanchez, P. Benit, P. Rustin, L.C. Lopez, I. Milosevic, and N. Raimundo. 2017. Acute and chronic mitochondrial respiratory chain deficiency differentially regulate lysosomal biogenesis. *Sci Rep*. 7:45076.

Fernandez-Mosquera, L., K.F. Yambire, R. Couto, L. Pereyra, K. Pabis, A.H. Ponsford, C.V. Diogo, M. Stagi, I. Milosevic, and N. Raimundo. 2019. Mitochondrial respiratory chain deficiency inhibits lysosomal hydrolysis. *Autophagy*. 15:1572-1591.

Filimonenko, M., P. Isakson, K.D. Finley, M. Anderson, H. Jeong, T.J. Melia, B.J. Bartlett, K.M. Myers, H.C. Birkeland, T. Lamark, D. Krainc, A. Brech, H. Stenmark, A. Simonsen, and A. Yamamoto. 2010. The selective macroautophagic degradation of aggregated proteins requires the PI3P-binding protein Alfy. *Mol Cell*. 38:265-279.

Finkbeiner, S. 2019. The Autophagy Lysosomal Pathway and Neurodegeneration. *Cold Spring Harbor perspectives in biology*.

Finn, R.D., A. Bateman, J. Clements, P. Coggill, R.Y. Eberhardt, S.R. Eddy, A. Heger, K. Hetherington, L. Holm, J. Mistry, E.L. Sonnhammer, J. Tate, and M. Punta. 2014. Pfam: the protein families database. *Nucleic Acids Res*. 42:D222-230.

Fitzpatrick, A.W.P., B. Falcon, S. He, A.G. Murzin, G. Murshudov, H.J. Garringer, R.A. Crowther, B. Ghetti, M. Goedert, and S.H.W. Scheres. 2017. Cryo-EM structures of tau filaments from Alzheimer's disease. *Nature*. 547:185-190.

Fraldi, A., A.D. Klein, D.L. Medina, and C. Settembre. 2016. Brain Disorders Due to Lysosomal Dysfunction. *Annu Rev Neurosci*. 39:277-295.

Frottin, F., F. Schueder, S. Tiwary, R. Gupta, R. Korner, T. Schlichthaerle, J. Cox, R. Jungmann, F.U. Hartl, and M.S. Hipp. 2019. The nucleolus functions as a phase-separated protein quality control compartment. *Science*. 365:342-347.

Glynn, M.W., and A.K. McAllister. 2006. Immunocytochemistry and quantification of protein colocalization in cultured neurons. *Nat Protoc*. 1:1287-1296.

Gruber, A., D. Hornburg, M. Antonin, N. Krahmer, J. Collado, M. Schaffer, G. Zubaite, C. Luchtenborg, T. Sachsenheimer, B. Brugger, M. Mann, W. Baumeister, F.U. Hartl, M.S. Hipp, and R. Fernandez-Busnadiego. 2018. Molecular and structural architecture of polyQ aggregates in yeast. *Proc Natl Acad Sci U S A*. 115:E3446-E3453.

Guo, Q., C. Lehmer, A. Martinez-Sanchez, T. Rudack, F. Beck, H. Hartmann, M. Perez-Berlanga, F. Frottin, M.S. Hipp, F.U. Hartl, D. Edbauer, W. Baumeister, and R. Fernandez-Busnadiego.

2018. In Situ Structure of Neuronal C9orf72 Poly-GA Aggregates Reveals Proteasome Recruitment. *Cell*. 172:696-705 e612.

Haass, C., and D.J. Selkoe. 2007. Soluble protein oligomers in neurodegeneration: lessons from the Alzheimer's amyloid beta-peptide. *Nat Rev Mol Cell Biol*. 8:101-112.

Harris, M.A., J. Clark, A. Ireland, J. Lomax, M. Ashburner, R. Foulger, K. Eilbeck, S. Lewis, B. Marshall, C. Mungall, J. Richter, G.M. Rubin, J.A. Blake, C. Bult, M. Dolan, H. Drabkin, J.T. Eppig, D.P. Hill, L. Ni, M. Ringwald, R. Balakrishnan, J.M. Cherry, K.R. Christie, M.C. Costanzo, S.S. Dwight, S. Engel, D.G. Fisk, J.E. Hirschman, E.L. Hong, R.S. Nash, A. Sethuraman, C.L. Theesfeld, D. Botstein, K. Dolinski, B. Feierbach, T. Berardini, S. Mundodi, S.Y. Rhee, R. Apweiler, D. Barrell, E. Camon, E. Dimmer, V. Lee, R. Chisholm, P. Gaudet, W. Kibbe, R. Kishore, E.M. Schwarz, P. Sternberg, M. Gwinn, L. Hannick, J. Wortman, M. Berriman, V. Wood, N. de la Cruz, P. Tonellato, P. Jaiswal, T. Seigfried, R. White, and C. Gene Ontology. 2004. The Gene Ontology (GO) database and informatics resource. *Nucleic Acids Res*. 32:D258-261.

Hartl, F.U. 2017. Protein Misfolding Diseases. *Annu Rev Biochem*. 86:21-26.

Hoffmann, A.C., G. Minakaki, S. Menges, R. Salvi, S. Savitskiy, A. Kazman, H. Vicente Miranda, D. Mielenz, J. Klucken, J. Winkler, and W. Xiang. 2019. Extracellular aggregated alpha synuclein primarily triggers lysosomal dysfunction in neural cells prevented by trehalose. *Sci Rep*. 9:544.

Hornburg, D., C. Drepper, F. Butter, F. Meissner, M. Sendtner, and M. Mann. 2014. Deep proteomic evaluation of primary and cell line motoneuron disease models delineates major differences in neuronal characteristics. *Mol Cell Proteomics*. 13:3410-3420.

Hosp, F., S. Gutierrez-Angel, M.H. Schaefer, J. Cox, F. Meissner, M.S. Hipp, F.U. Hartl, R. Klein, I. Dudanova, and M. Mann. 2017. Spatiotemporal Proteomic Profiling of Huntington's Disease Inclusions Reveals Widespread Loss of Protein Function. *Cell Rep*. 21:2291-2303.

Hrabe, T., Y. Chen, S. Pfeffer, L. Kuhn Cuellar, A.-V. Mangold, and F. Förster. 2012. PyTom: A python-based toolbox for localization of macromolecules in cryo-electron tomograms and subtomogram analysis. *Journal of structural biology*. 178:177-188.

Jiang, M., and G. Chen. 2006. High Ca2+-phosphate transfection efficiency in low-density neuronal cultures. *Nat Protoc*. 1:695-700.

Jo, C., S. Gundemir, S. Pritchard, Y.N. Jin, I. Rahman, and G.V. Johnson. 2014. Nrf2 reduces levels of phosphorylated tau protein by inducing autophagy adaptor protein NDP52. *Nat Commun*. 5:3496.

Kantheti, P., X. Qiao, M.E. Diaz, A.A. Peden, G.E. Meyer, S.L. Carskadon, D. Kapfhamer, D. Sufalko, M.S. Robinson, J.L. Noebels, and M. Burmeister. 1998. Mutation in AP-3 delta in the mocha mouse links endosomal transport to storage deficiency in platelets, melanosomes, and synaptic vesicles. *Neuron*. 21:111-122.

Kent, H.M., P.R. Evans, I.B. Schafer, S.R. Gray, C.M. Sanderson, J.P. Luzio, A.A. Peden, and D.J. Owen. 2012. Structural basis of the intracellular sorting of the SNARE VAMP7 by the AP3 adaptor complex. *Dev Cell*. 22:979-988.

Khatter, H., A.G. Myasnikov, S.K. Natchiar, and B.P. Klaholz. 2015. Structure of the human 80S ribosome. *Nature*. 520:640-645.

Kim, Y.E., F. Hosp, F. Frottin, H. Ge, M. Mann, M. Hayer-Hartl, and F.U. Hartl. 2016. Soluble Oligomers of PolyQ-Expanded Huntingtin Target a Multiplicity of Key Cellular Factors. *Mol Cell*. 63:951-964.

Kremer, J.R., D.N. Mastronarde, and J.R. McIntosh. 1996. Computer visualization of three-dimensional image data using IMOD. *J Struct Biol*. 116:71-76.

Lamark, T., and T. Johansen. 2012. Aggrephagy: selective disposal of protein aggregates by macroautophagy. *Int J Cell Biol*. 2012:736905.

Leeman, D.S., K. Hebestreit, T. Ruetz, A.E. Webb, A. McKay, E.A. Pollina, B.W. Dulken, X. Zhao, R.W. Yeo, T.T. Ho, S. Mahmoudi, K. Devarajan, E. Passegue, T.A. Rando, J. Frydman, and A. Brunet. 2018. Lysosome activation clears aggregates and enhances quiescent neural stem cell activation during aging. *Science*. 359:1277-1283.

Li, P., S.A. Merrill, E.M. Jorgensen, and K. Shen. 2016. Two Clathrin Adaptor Protein Complexes Instruct Axon-Dendrite Polarity. *Neuron*. 90:564-580.

Li, X., P. Mooney, S. Zheng, C.R. Booth, M.B. Braunfeld, S. Gubbens, D.A. Agard, and Y. Cheng. 2013. Electron counting and beam-induced motion correction enable near-atomic-resolution single-particle cryo-EM. *Nat Methods*. 10:584-590.

Louis, J.V., E. Martens, P. Borghgraef, C. Lambrecht, W. Sents, S. Longin, K. Zwaenepoel, R. Pijnenborg, I. Landrieu, G. Lippens, B. Ledermann, J. Gotz, F. Van Leuven, J. Goris, and V. Janssens. 2011. Mice lacking phosphatase PP2A subunit PR61/B'delta (Ppp2r5d) develop

spatially restricted tauopathy by deregulation of CDK5 and GSK3beta. *Proc Natl Acad Sci U S A*. 108:6957-6962.

Martinez-Sanchez, A., I. Garcia, S. Asano, V. Lucic, and J.J. Fernandez. 2014. Robust membrane detection based on tensor voting for electron tomography. *J Struct Biol*. 186:49-61.

Mastronarde, D.N. 2005. Automated electron microscope tomography using robust prediction of specimen movements. *J Struct Biol*. 152:36-51.

May, S., D. Hornburg, M.H. Schludi, T. Arzberger, K. Rentzsch, B.M. Schwenk, F.A. Grasser, K. Mori, E. Kremmer, J. Banzhaf-Strathmann, M. Mann, F. Meissner, and D. Edbauer. 2014. C9orf72 FTLD/ALS-associated Gly-Ala dipeptide repeat proteins cause neuronal toxicity and Unc119 sequestration. *Acta Neuropathol*. 128:485-503.

Mazzulli, J.R., F. Zunke, O. Isacson, L. Studer, and D. Krainc. 2016. alpha-Synuclein-induced lysosomal dysfunction occurs through disruptions in protein trafficking in human midbrain synucleinopathy models. *Proc Natl Acad Sci U S A*. 113:1931-1936.

Menzies, F.M., A. Fleming, and D.C. Rubinsztein. 2015. Compromised autophagy and neurodegenerative diseases. *Nat Rev Neurosci*. 16:345-357.

Newell-Litwa, K., E. Seong, M. Burmeister, and V. Faundez. 2007. Neuronal and non-neuronal functions of the AP-3 sorting machinery. *J Cell Sci*. 120:531-541.

Nixon, R.A. 2020. The aging lysosome: An essential catalyst for late-onset neurodegenerative diseases. *Biochim Biophys Acta Proteins Proteom*. 1868:140443.

Ohno, H., R.C. Aguilar, D. Yeh, D. Taura, T. Saito, and J.S. Bonifacino. 1998. The medium subunits of adaptor complexes recognize distinct but overlapping sets of tyrosine-based sorting signals. *J Biol Chem*. 273:25915-25921.

Olsen, J.V., B. Macek, O. Lange, A. Makarov, S. Horning, and M. Mann. 2007. Higher-energy C-trap dissociation for peptide modification analysis. *Nat Methods*. 4:709-712.

Olzscha, H., S.M. Schermann, A.C. Woerner, S. Pinkert, M.H. Hecht, G.G. Tartaglia, M. Vendruscolo, M. Hayer-Hartl, F.U. Hartl, and R.M. Vabulas. 2011. Amyloid-like aggregates sequester numerous metastable proteins with essential cellular functions. *Cell*. 144:67-78.

Peden, A.A., V. Oorschot, B.A. Hesser, C.D. Austin, R.H. Scheller, and J. Klumperman. 2004. Localization of the AP-3 adaptor complex defines a novel endosomal exit site for lysosomal membrane proteins. *J Cell Biol*. 164:1065-1076.

Peden, A.A., R.E. Rudge, W.W. Lui, and M.S. Robinson. 2002. Assembly and function of AP-3 complexes in cells expressing mutant subunits. *J Cell Biol*. 156:327-336.

Platt, F.M., A. d'Azzo, B.L. Davidson, E.F. Neufeld, and C.J. Tifft. 2018. Lysosomal storage diseases. *Nat Rev Dis Primers*. 4:27.

Poole, B., and S. Ohkuma. 1981. Effect of weak bases on the intralysosomal pH in mouse peritoneal macrophages. *J Cell Biol*. 90:665-669.

Rigort, A., F.J. Bauerlein, A. Leis, M. Gruska, C. Hoffmann, T. Laugks, U. Bohm, M. Eibauer, H. Gnaegi, W. Baumeister, and J.M. Plitzko. 2010. Micromachining tools and correlative approaches for cellular cryo-electron tomography. *J Struct Biol*. 172:169-179.

Rigort, A., F.J. Bauerlein, E. Villa, M. Eibauer, T. Laugks, W. Baumeister, and J.M. Plitzko. 2012. Focused ion beam micromachining of eukaryotic cells for cryoelectron tomography. *Proc Natl Acad Sci U S A*. 109:4449-4454.

Rovelet-Lecrux, A., C. Charbonnier, D. Wallon, G. Nicolas, M.N. Seaman, C. Pottier, S.Y. Breusegem, P.P. Mathur, P. Jenardhanan, K. Le Guennec, A.S. Mukadam, O. Quenez, S. Coutant, S. Rousseau, A.C. Richard, A. Boland, J.F. Deleuze, T. Frebourg, D. Hannequin, D. Campion, and C.-M. collaborators. 2015. De novo deleterious genetic variations target a biological network centered on Abeta peptide in early-onset Alzheimer disease. *Mol Psychiatry*. 20:1046-1056.

Ruepp, A., B. Waegele, M. Lechner, B. Brauner, I. Dunger-Kaltenbach, G. Fobo, G. Frishman, C. Montrone, and H.W. Mewes. 2010. CORUM: the comprehensive resource of mammalian protein complexes--2009. *Nucleic Acids Res*. 38:D497-501.

Sardiello, M., M. Palmieri, A. di Ronza, D.L. Medina, M. Valenza, V.A. Gennarino, C. Di Malta, F. Donaudy, V. Embrione, R.S. Polishchuk, S. Banfi, G. Parenti, E. Cattaneo, and A. Ballabio. 2009. A gene network regulating lysosomal biogenesis and function. *Science*. 325:473-477.

Saudou, F., and S. Humbert. 2016. The Biology of Huntingtin. *Neuron*. 89:910-926.

Schindelin, J., I. Arganda-Carreras, E. Frise, V. Kaynig, M. Longair, T. Pietzsch, S. Preibisch, C. Rueden, S. Saalfeld, B. Schmid, J.Y. Tinevez, D.J. White, V. Hartenstein, K. Eliceiri, P. Tomancak, and A. Cardona. 2012. Fiji: an open-source platform for biological-image analysis. *Nat Methods*. 9:676-682.

Settembre, C., C. Di Malta, V.A. Polito, M. Garcia Arencibia, F. Vetrini, S. Erdin, S.U. Erdin, T. Huynh, D. Medina, P. Colella, M. Sardiello, D.C. Rubinsztein, and A. Ballabio. 2011. TFEB links autophagy to lysosomal biogenesis. *Science*. 332:1429-1433.

Settembre, C., A. Fraldi, D.L. Medina, and A. Ballabio. 2013. Signals from the lysosome: a control centre for cellular clearance and energy metabolism. *Nat Rev Mol Cell Biol*. 14:283-296.

Shirasaki, D.I., E.R. Greiner, I. Al-Ramahi, M. Gray, P. Boontheung, D.H. Geschwind, J. Botas, G. Coppola, S. Horvath, J.A. Loo, and X.W. Yang. 2012. Network organization of the huntingtin proteomic interactome in mammalian brain. *Neuron*. 75:41-57.

Soto, C., and S. Pritzkow. 2018. Protein misfolding, aggregation, and conformational strains in neurodegenerative diseases. *Nature neuroscience*. 21:1332-1340.

Spaet, R.H., D.J. Sullivan, and R.M. Diener. 1983. Occurrence of myeloid bodies in rats following two-year administration of imipramine hydrochloride. *Toxicol Pathol*. 11:3-11.

Suzuki, K., and R.D. Terry. 1967. Fine structural localization of acid phosphatase in senile plaques in Alzheimer's presenile dementia. *Acta Neuropathol*. 8:276-284.

Swank, R.T., M. Reddington, O. Howlett, and E.K. Novak. 1991. Platelet storage pool deficiency associated with inherited abnormalities of the inner ear in the mouse pigment mutants muted and mocha. *Blood*. 78:2036-2044.

Taylor, J.P., R.H. Brown, Jr., and D.W. Cleveland. 2016. Decoding ALS: from genes to mechanism. *Nature*. 539:197-206.

Trinkaus, V.A., I. Riera-Tur, A. Martinez-Sanchez, F.J.B. Bauerlein, Q. Guo, T. Arzberger, W. Baumeister, I. Dudanova, M.S. Hipp, F.U. Hartl, and R. Fernandez-Busnadiego. 2021. In situ architecture of neuronal alpha-Synuclein inclusions. *Nat Commun*. 12:2110.

Usenovic, M., E. Tresse, J.R. Mazzulli, J.P. Taylor, and D. Krainc. 2012. Deficiency of ATP13A2 leads to lysosomal dysfunction, alpha-synuclein accumulation, and neurotoxicity. *J Neurosci*. 32:4240-4246.

Vincenz-Donnelly, L., H. Holthusen, R. Korner, E.C. Hansen, J. Presto, J. Johansson, R. Sawarkar, F.U. Hartl, and M.S. Hipp. 2018. High capacity of the endoplasmic reticulum to prevent secretion and aggregation of amyloidogenic proteins. *EMBO J*. 37:337-350.

Wagner, J., M. Schaffer, and R. Fernandez-Busnadiego. 2017. Cryo-electron tomography-the cell biology that came in from the cold. *FEBS Lett*. 591:2520-2533.

Wang, C., M.A. Telpoukhovskaia, B.A. Bahr, X. Chen, and L. Gan. 2018. Endo-lysosomal dysfunction: a converging mechanism in neurodegenerative diseases. *Curr Opin Neurobiol*. 48:52-58.

Wei, Y., T. Liu, S.L. Sazinsky, D.A. Moffet, I. Pelczer, and M.H. Hecht. 2003. Stably folded de novo proteins from a designed combinatorial library. *Protein Sci*. 12:92-102.

West, M.W., W. Wang, J. Patterson, J.D. Mancias, J.R. Beasley, and M.H. Hecht. 1999. De novo amyloid proteins from designed combinatorial libraries. *Proc Natl Acad Sci U S A*. 96:11211-11216.

Winklhofer, K.F., J. Tatzelt, and C. Haass. 2008. The two faces of protein misfolding: gain- and loss-of-function in neurodegenerative diseases. *EMBO J*. 27:336-349.

Winner, B., R. Jappelli, S.K. Maji, P.A. Desplats, L. Boyer, S. Aigner, C. Hetzer, T. Loher, M. Vilar, S. Campioni, C. Tzitzilonis, A. Soragni, S. Jessberger, H. Mira, A. Consiglio, E. Pham, E. Masliah, F.H. Gage, and R. Riek. 2011. In vivo demonstration that alpha-synuclein oligomers are toxic. *Proc Natl Acad Sci U S A*. 108:4194-4199.

Winslow, A.R., C.W. Chen, S. Corrochano, A. Acevedo-Arozena, D.E. Gordon, A.A. Peden, M. Lichtenberg, F.M. Menzies, B. Ravikumar, S. Imarisio, S. Brown, C.J. O'Kane, and D.C. Rubinsztein. 2010. alpha-Synuclein impairs macroautophagy: implications for Parkinson's disease. *J Cell Biol*. 190:1023-1037.

Woerner, A.C., F. Frottin, D. Hornburg, L.R. Feng, F. Meissner, M. Patra, J. Tatzelt, M. Mann, K.F. Winklhofer, F.U. Hartl, and M.S. Hipp. 2016. Cytoplasmic protein aggregates interfere with nucleocytoplasmic transport of protein and RNA. *Science*. 351:173-176.

Wong, Y.C., and E.L. Holzbaur. 2014. The regulation of autophagosome dynamics by huntingtin and HAP1 is disrupted by expression of mutant huntingtin, leading to defective cargo degradation. *J Neurosci*. 34:1293-1305.

Yamamoto, A., and Z. Yue. 2014. Autophagy and its normal and pathogenic states in the brain. *Annu Rev Neurosci*. 37:55-78.

Yang, H., and H.Y. Hu. 2016. Sequestration of cellular interacting partners by protein aggregates: implication in a loss-of-function pathology. *The FEBS journal*. 283:3705-3717.

Zhang, W., A. Tarutani, K.L. Newell, A.G. Murzin, T. Matsubara, B. Falcon, R. Vidal, H.J. Garringer, Y. Shi, T. Ikeuchi, S. Murayama, B. Ghetti, M. Hasegawa, M. Goedert, and S.H.W. Scheres. 2020. Novel tau filament fold in corticobasal degeneration. *Nature*. 580:283-287.

Zhou, C., B.D. Slaughter, J.R. Unruh, F. Guo, Z. Yu, K. Mickey, A. Narkar, R.T. Ross, M. McClain, and R. Li. 2014. Organelle-based aggregation and retention of damaged proteins in asymmetrically dividing cells. *Cell*. 159:530-542.

Figures

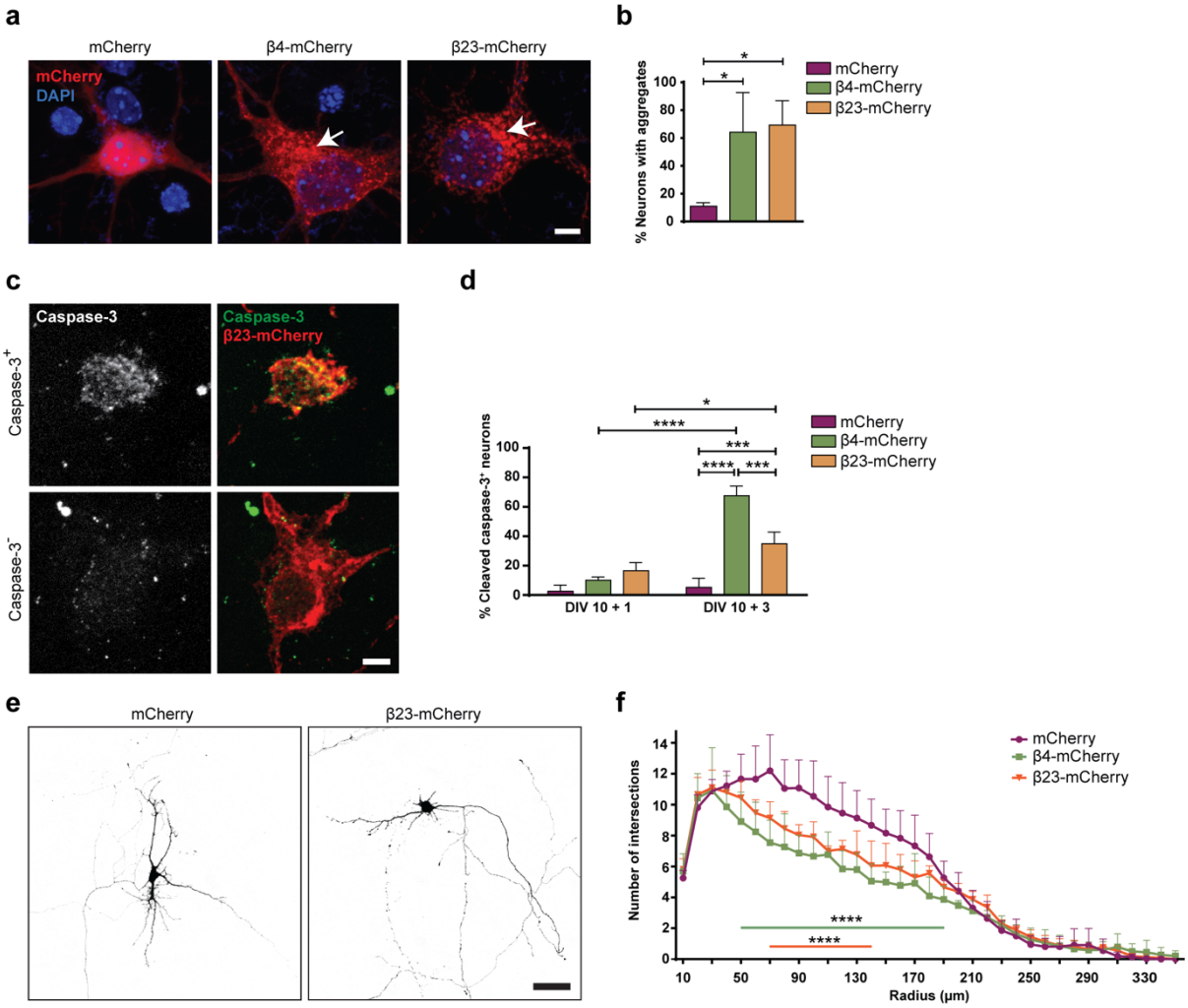

Figure 1. β proteins aggregate and cause toxicity in transfected primary neurons. **a**, Transfected cortical neurons at DIV 10+1. Arrows point to β protein aggregates. **b**, Percentage of transfected neurons bearing aggregates at DIV 10+1 (n=3 independent experiments, 25-45 cells/condition/experiment; One-way ANOVA with Dunnett's post hoc test). **c**, Examples of DIV10+1 β23-mCherry neurons positive (top) and negative (bottom) for cleaved caspase-3. **d**, Percentage of transfected neurons positive for cleaved caspase-3 (n=3 independent experiments, 25-45 cells/condition/experiment; Two-way ANOVA with Tukey's post hoc test). **e**, Examples of primary hippocampal neurons transfected with mCherry or β23-mCherry at DIV 10+2. Images are colour-inverted with mCherry fluorescence shown in black. Note that the β23-mCherry cell has fewer primary dendrites. **f**, Sholl analysis reveals reduced dendritic complexity in the presence of β proteins (n=3 independent experiments, 10-30 cells/condition/experiment; Two-way ANOVA with Tukey's post hoc test). *p<0.05; ***p<0.001; ****p<0.0001. Scale bars, 5 μm in **a** and **c**; 50 μm in **e**.

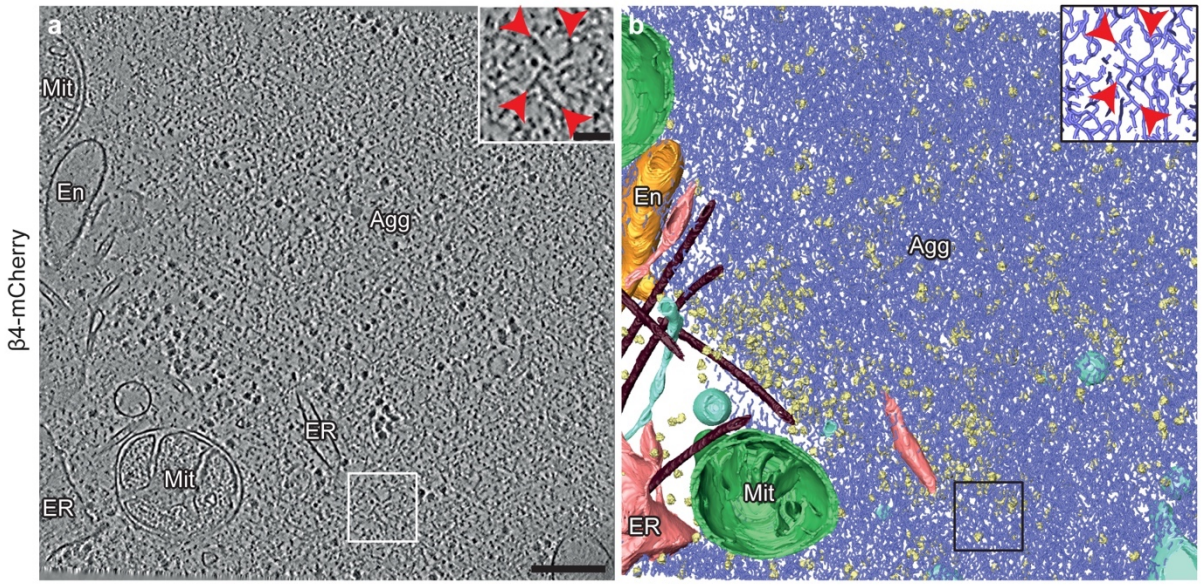

Figure 2. Ultrastructure of β protein aggregates in primary neurons. a, Tomographic slice of a β4-mCherry aggregate in a transfected DIV 6+1 cortical neuron. The area marked by the box is magnified in the inset. Red arrowheads point to β4-mCherry fibrils. Agg, β4-mCherry aggregate; En, endosome; ER, endoplasmic reticulum; Mit, mitochondrion. **b**, 3D rendering of the tomogram shown in **a**. β4-mCherry fibrils, blue; mitochondria, green; ER membranes, salmon; endosome, gold; vesicles, cyan; ribosomes, yellow; microtubules, brown. Scale bars in **a**, 200 nm and 50 nm (inset).

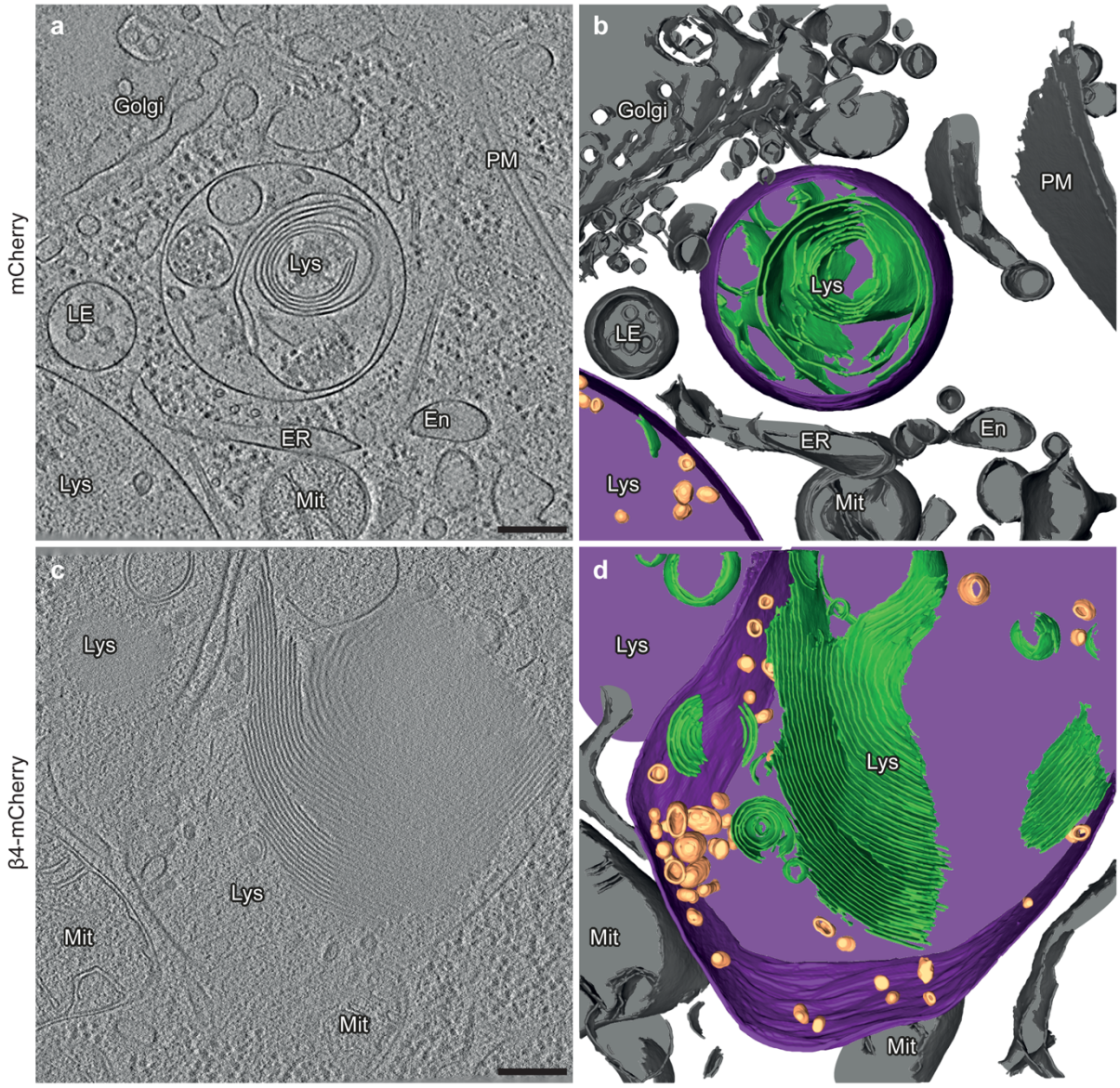

Figure 3. Aberrant lysosomal ultrastructure in β protein-expressing neurons. a, Example of a lysosome in a tomogram from a DIV 6+1 cortical neuron transfected with mCherry. **c**, Example of a lysosome in a neuron transfected with β4-mCherry. Note the presence of abundant membrane stacks and electron-dense material within the lysosome. En, endosome; ER, endoplasmic reticulum; LE, late endosome; Lys, lysosome; Mit, mitochondrion; PM, plasma membrane. **b**, **d**, 3D rendering of the tomograms shown in **a** and **c**, respectively. Lysosomal membrane, purple; membrane stacks within the lysosomes, green; intraluminal vesicles, gold; other cellular membranes, grey. For additional examples see Supplementary Fig. S4. Scale bars in **a** and **c**, 200 nm.

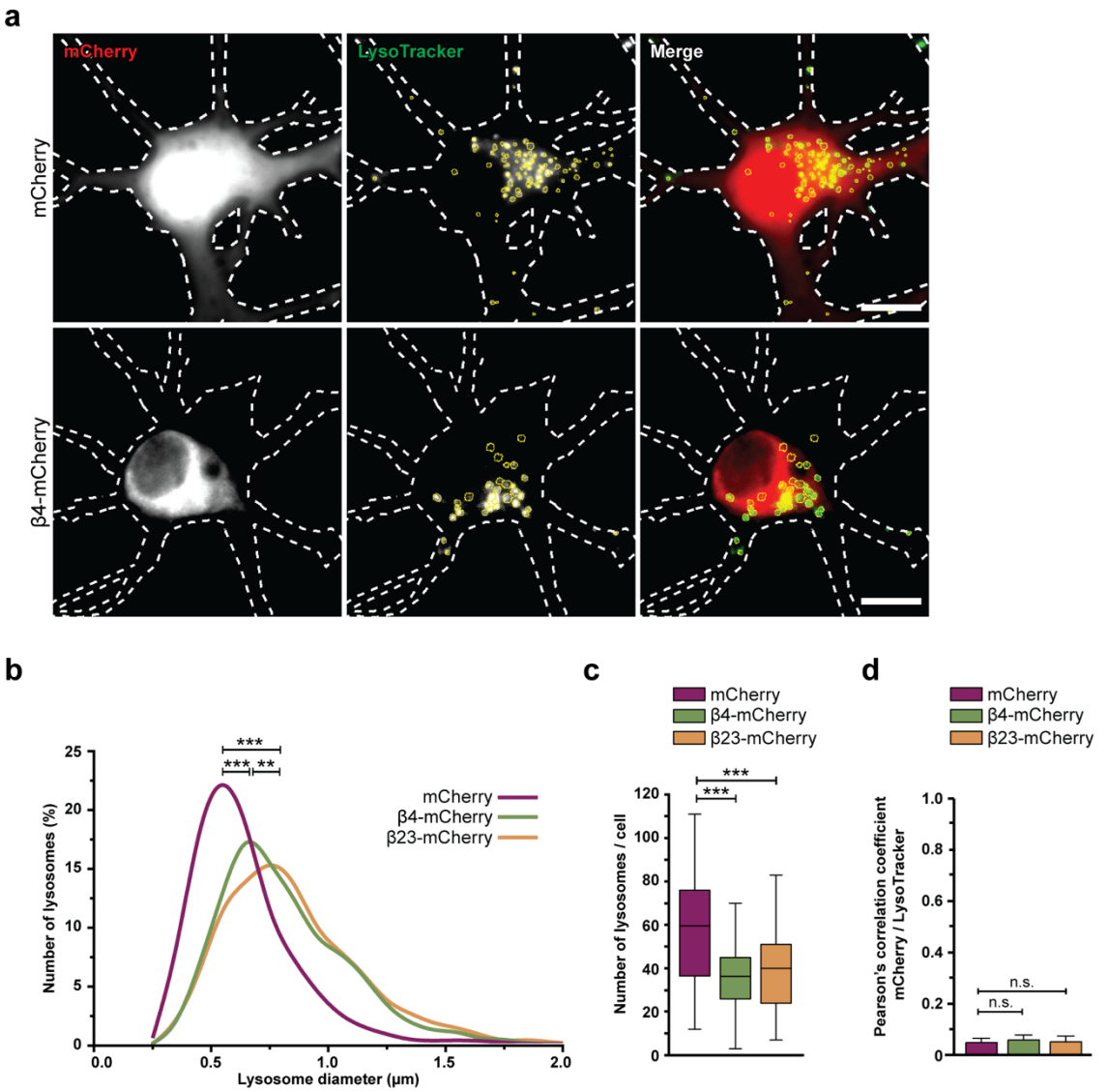

Figure 4. Defects of lysosomal morphology in the presence of β proteins. a, Fluorescent images of DIV 6+1 primary cortical neurons transfected with mCherry (top) or β4-mCherry (bottom) and incubated with LysoTracker Green. White dashed lines show the contours of the neuron. Yellow circles outline lysosomes. **b**, Distribution of the lysosomal size in control and β protein-expressing neurons (mCherry, n=2148 lysosomes from 36 cells; β4-mCherry, n=1595 lysosomes from 44 cells; β23-mCherry, n=1838 lysosomes from 46 cells; from 4 independent experiments; Two-tailed Mann-Whitney test). **c**, Box plot showing the number of lysosomes per neuron (mCherry, n=36 cells; β4-mCherry, n=44 cells; β23-mCherry, n=46 cells; from 4 independent experiments; Two-tailed Mann-Whitney test). **d**, Quantification of Person's correlation coefficient between the mCherry and LysoTracker signal (n=39 β4-mCherry cells, 36 β23-mCherry cells and 36 mCherry cells; One-way ANOVA with Tukey's post hoc test). **p<0.01; ***p<0.001, n.s. – not significant. Scale bars in **a**, 10 μm.

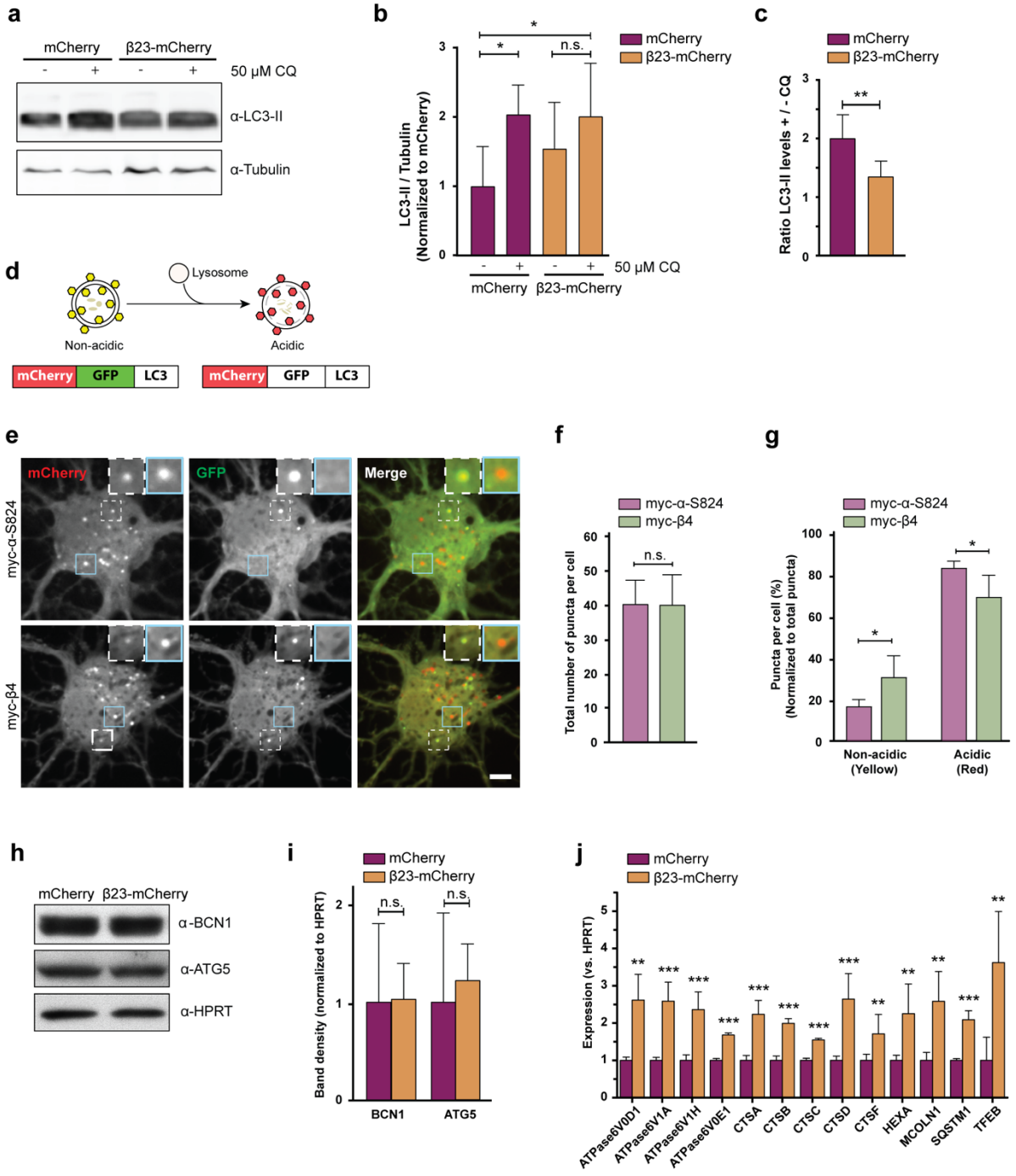

Figure 5. β proteins impair autophagy. a, Western blot for LC3B-II in HeLa cell lysates under control conditions, upon treatment with 50 μM Chloroquine (CQ), and/or starvation in EBSS medium. Tubulin was used as a loading control. **b**, Quantification of LC3B-II levels. All conditions were normalized to mCherry (n=6 independent experiments; One-way ANOVA with Tukey's multiple comparison test). **c,** Quantification of the ratio of LC3B-II levels in cells treated or not treated with CQ. Same data was analysed as shown in **b** (n=6 independent experiments; Two-tailed t-test with Welch's correction). **d**, mCherry-GFP-LC3 reporter appears yellow in non-acidic and red in acidic organelles due to quenching of GFP fluorescence at low pH. **e**, Live single plane images of the reporter signal in DIV 10+3 neuronal cultures transfected with myc-α-S824 (top) and myc-β4 (bottom). Examples of non-acidic and acidic organelles are indicated with white and blue boxes, respectively, and shown at higher magnification in the insets. **f**, Quantification of the total number of reporter puncta per cell (n=4 independent experiments; 15-45 cells/condition/experiment; Two-tailed t-test with Welch correction). **g**, Quantification of the fraction of non-acidic (yellow puncta) and acidic (red only puncta); (same cells

were analysed as in **f**; Two-way ANOVA with Sidak's post hoc test). **h**, Western blots for early autophagy markers in lysates of HeLa cells transfected with mCherry or β23-mCherry. HPRT was used as a loading control. **i**, Western blot quantification (n=5 independent experiments; Two-tailed t-test). **j**, Transcript levels of lysosomal genes in mCherry or β23-mCherry HeLa cells determined with RT-PCR (n=6 experiments; Two-tailed t-test). *p<0.05; **p<0.01; ***p<0.001; n.s. – not significant. Scale bar in **e**, 5 µm.

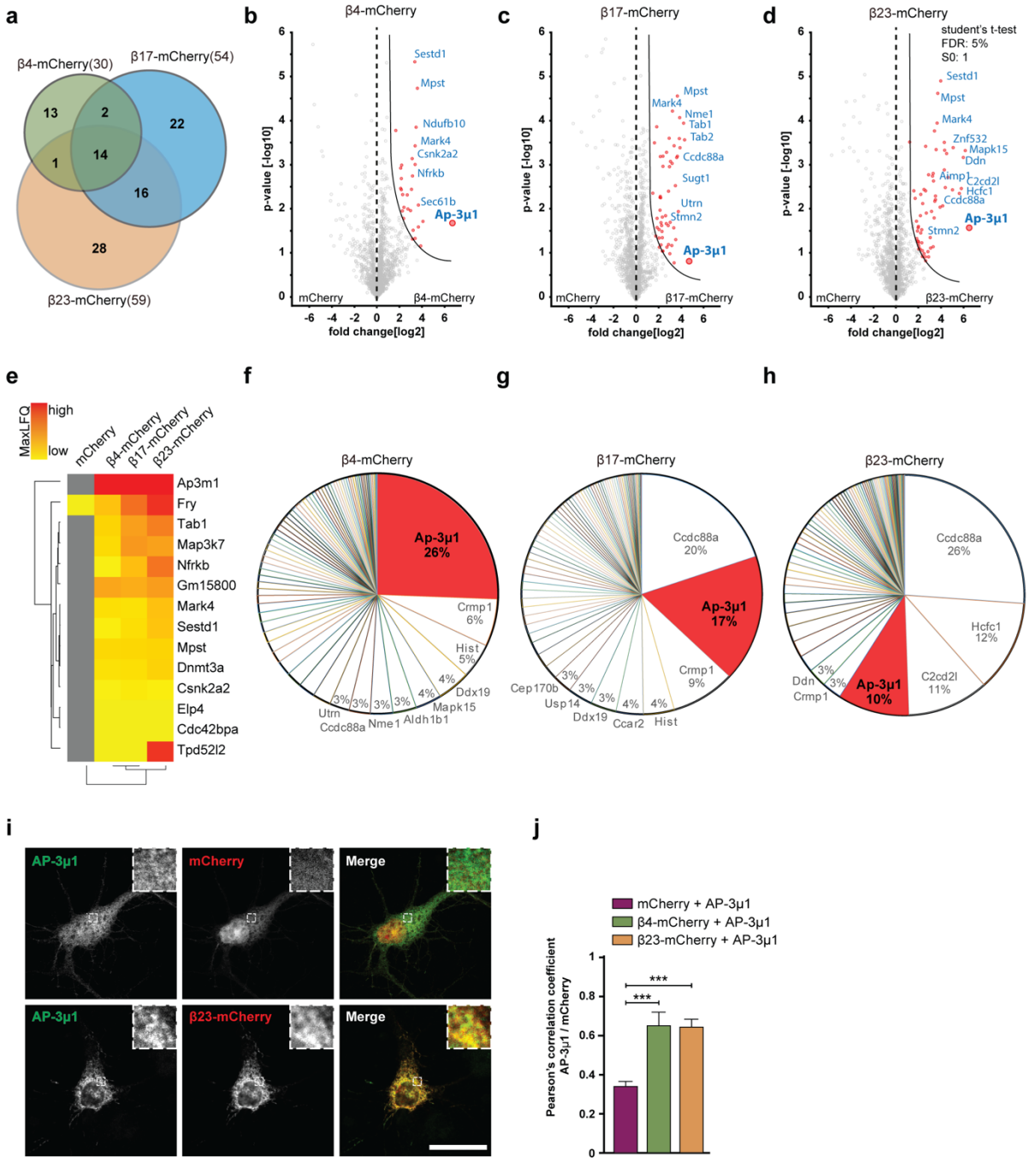

Figure 6. β protein interactome in primary neurons. a, Venn diagram depicting numbers and overlap of interactors for the three β proteins investigated. **b-d**, Volcano plots depicting proteins significantly enriched in β protein IPs. Red dots denote proteins that pass 5% permutation-based FDR (curved line on the right; proteins significantly associated with mCherry are not highlighted for the interactomes). **e**, Heat map of common interactors of all three β proteins. **f-h**, Pie charts showing the quantitative composition of β protein-interacting complex. **i**, Single confocal plane images of DIV 6+1 cortical neurons co-transfected with AP-3µ1 and either mCherry (top) or β23-mCherry (bottom). Anti-Flag staining was used to detect AP-3µ1. The areas marked by the boxes are magnified in the insets. **j**, Quantification of Person's correlation coefficient between the AP-3µ1 and mCherry or AP-3µ1 and β protein signal (n=3 independent experiments, 10-30 cells/condition/experiment; One-way ANOVA with Tukey's post hoc test). ***p<0.001. Scale bar in **i**, 10 µm.

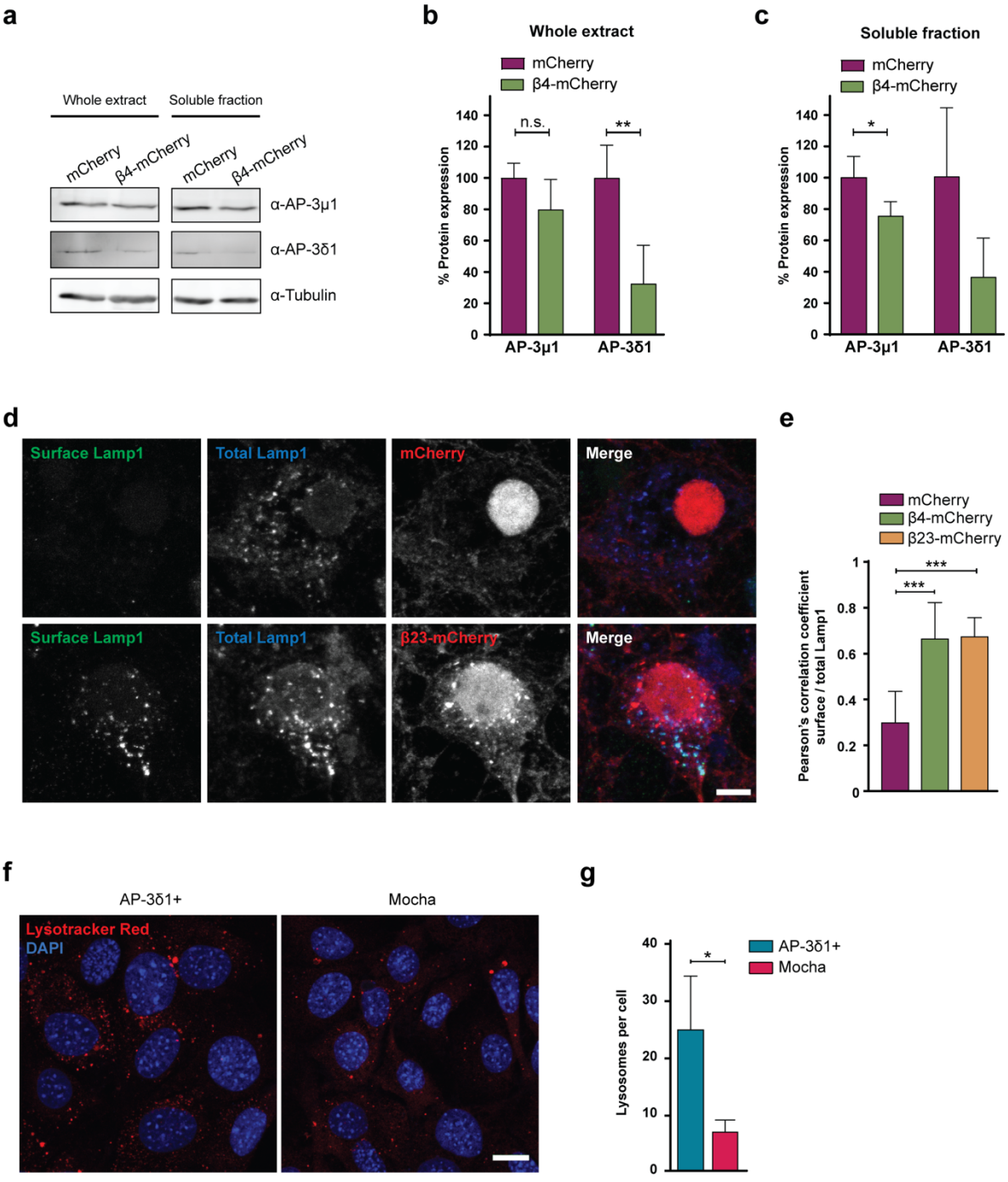

Figure 7. Dysfunction of the AP-3 complex causes missorting of Lamp1 and lysosomal defects. **a**, Western blots for AP-3 subunits in whole lysates (left) and Triton-X-soluble fractions (right) of DIV 10+6 primary neurons transduced with mCherry or β4-mCherry. Tubulin was used as a loading control. **b-c**, Quantification of **a**. Levels of AP-3 subunits were first normalized to tubulin, then values for β4-mCherry neurons were normalized to those of mCherry neurons and expressed as percentage (n=4 independent cultures; Two-tailed t-test with Welch's correction). **d**, Maximum intensity projections of DIV 10+4 neurons transduced with mCherry (top) or β4-mCherry (bottom) and stained for surface (green) and total (red) Lamp1. **e**, Quantification of Pearson's correlation coefficient between surface and total Lamp1 signal (n=6 independent experiments, 25 cells/condition/experiment; One-way ANOVA with Dunnett's post hoc test). **f**, Fluorescent images of control (left) and mocha cells (right) incubated with LysoTracker Red. Nuclei were labelled with DAPI (blue). **g**, Quantification of lysosome numbers per cell (n=4 independent experiments; at least 100 cells/condition/experiment; Two-tailed t-test with Welch correction). *p<0.05, **p<0.01; ***p<0.001. Scale bars; **d**, 10 μm; **f**, 20 μm.

Supplementary figures

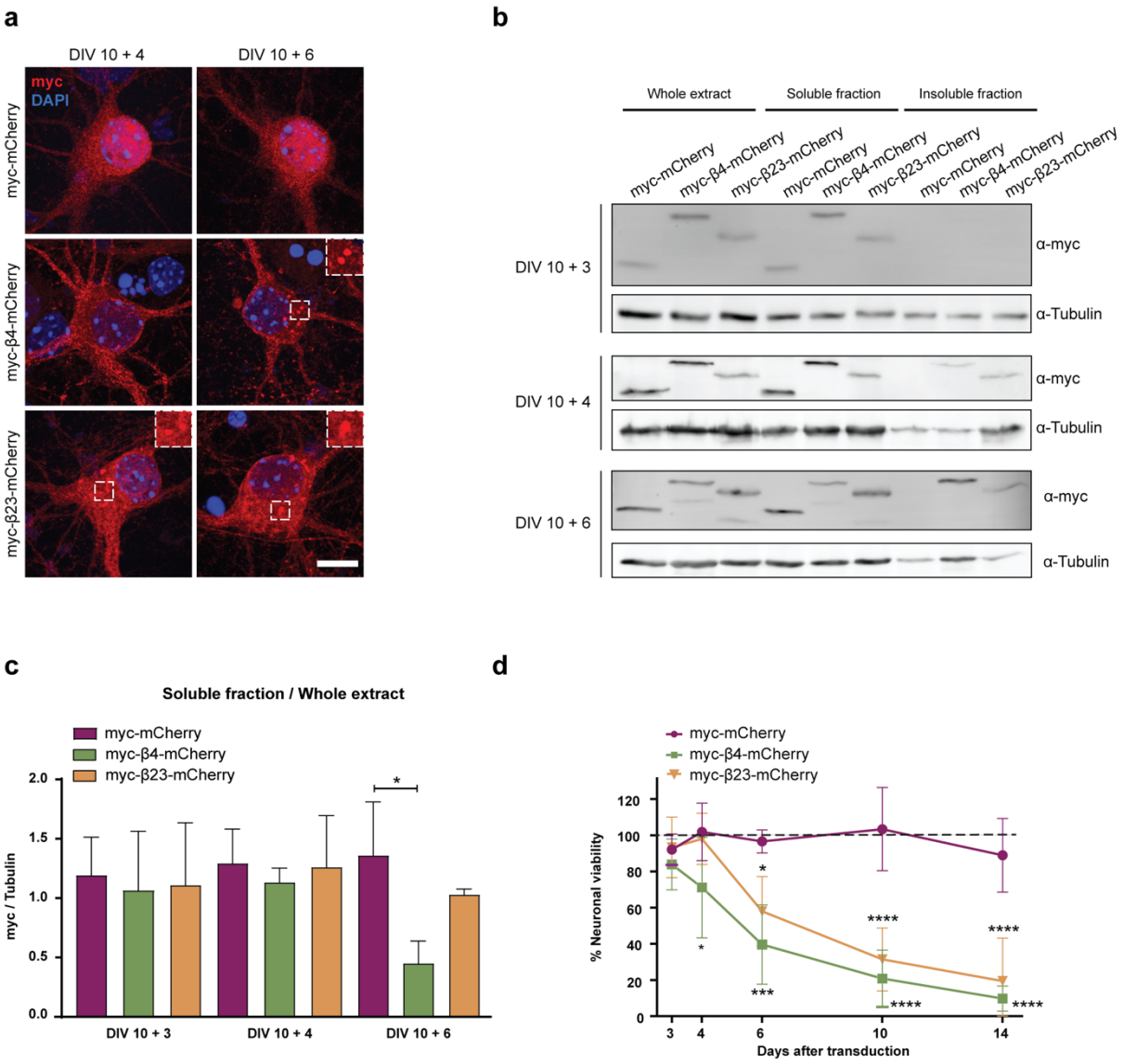

Supplementary Figure S1. Lentiviral transduction of β proteins leads to aggregation and toxicity in primary neurons. a, Primary cortical neurons transduced with mCherry or with β proteins at indicated time points. Transduced proteins were visualized by myc staining. Insets show examples of β protein aggregates. **b**, Western blot showing mCherry and β proteins in the whole cell extract, soluble, and insoluble fraction of lentivirally transduced neurons at DIV 10+3 (top), DIV 10+4 (middle) and DIV 10+6 (bottom). Tubulin was used as a loading control. The amount of proteins in the pellet fraction (shown below the blots) was quantified by normalizing the myc band intensity in the pellet to the band intensity in the soluble fraction for each corresponding condition. **c-d**, Quantification of mCherry, β4-mCherry and β23-mCherry levels in the soluble fraction (n=4 Western blots from 3 independent DIV 10+3 cultures, 4 independent DIV 10+4 cultures, and 3 independent DIV 10+6 cultures; One-way ANOVA with Dunnett's post hoc test). **d**, Quantification of neuronal survival determined by MTT assay at the indicated time points (n=4 independent experiments; Two-way ANOVA with Tukey's post hoc test). *p<0.05; ***p<0.001; ****p<0.0001; n.s. – not significant. Scale bar in **a**, 5 µm.

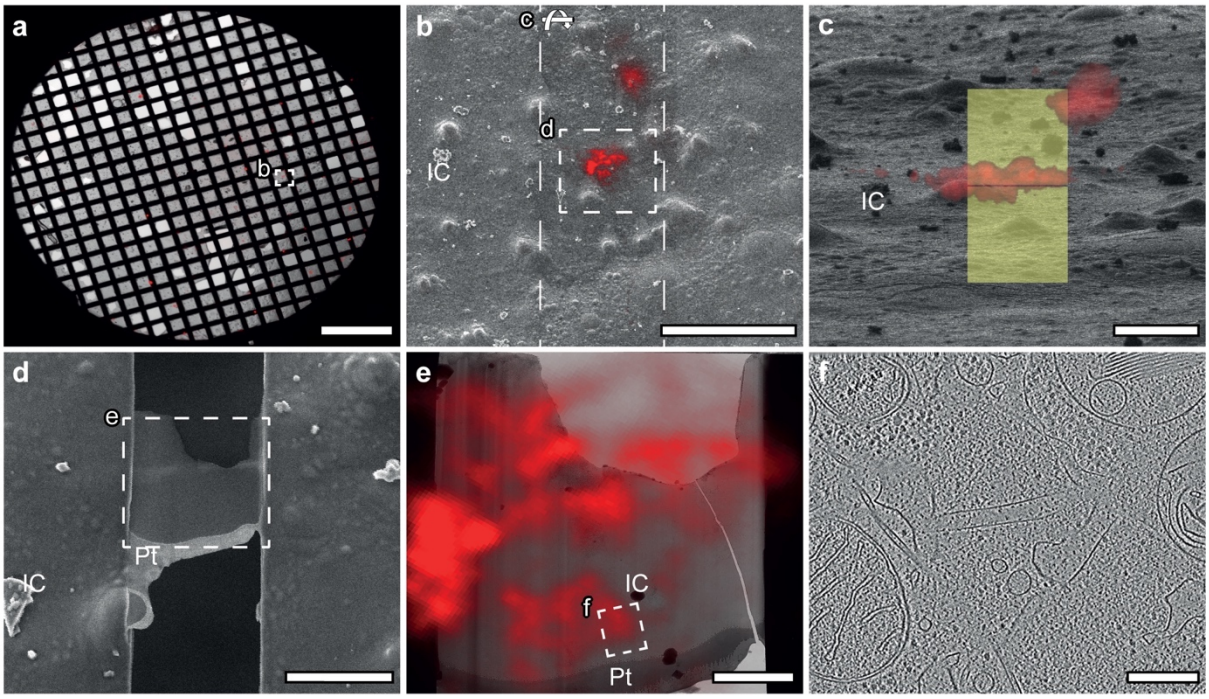

Supplementary Figure S2. Cryo-electron tomography sample preparation workflow. a, Vitrified cells on EM grids are imaged by cryo-light microscopy and cells of interest are identified. **b**, Grids are transferred to a cryo-FIB / scanning electron microscope (SEM) and positions of cells of interest are found via cryo-light microscopy (LM) / cryo-SEM correlation. **c**-**d**, Cells are thinned to a thickness of max. 200 nm by means of FIB milling. **e**, Grids are transferred to a cryo-transmission electron microscope (TEM) and regions of interest are identified via cryo-LM / cryo-TEM correlation and **f**, imaged by cryo-electron tomography. IC, ice contamination; Pt, platinum coating. Scale bars in **a**, 500 µm; **b**, 50 µm; **c** and **d**, 10 µm; **e**, 3 µm; **f**, 200 nm.

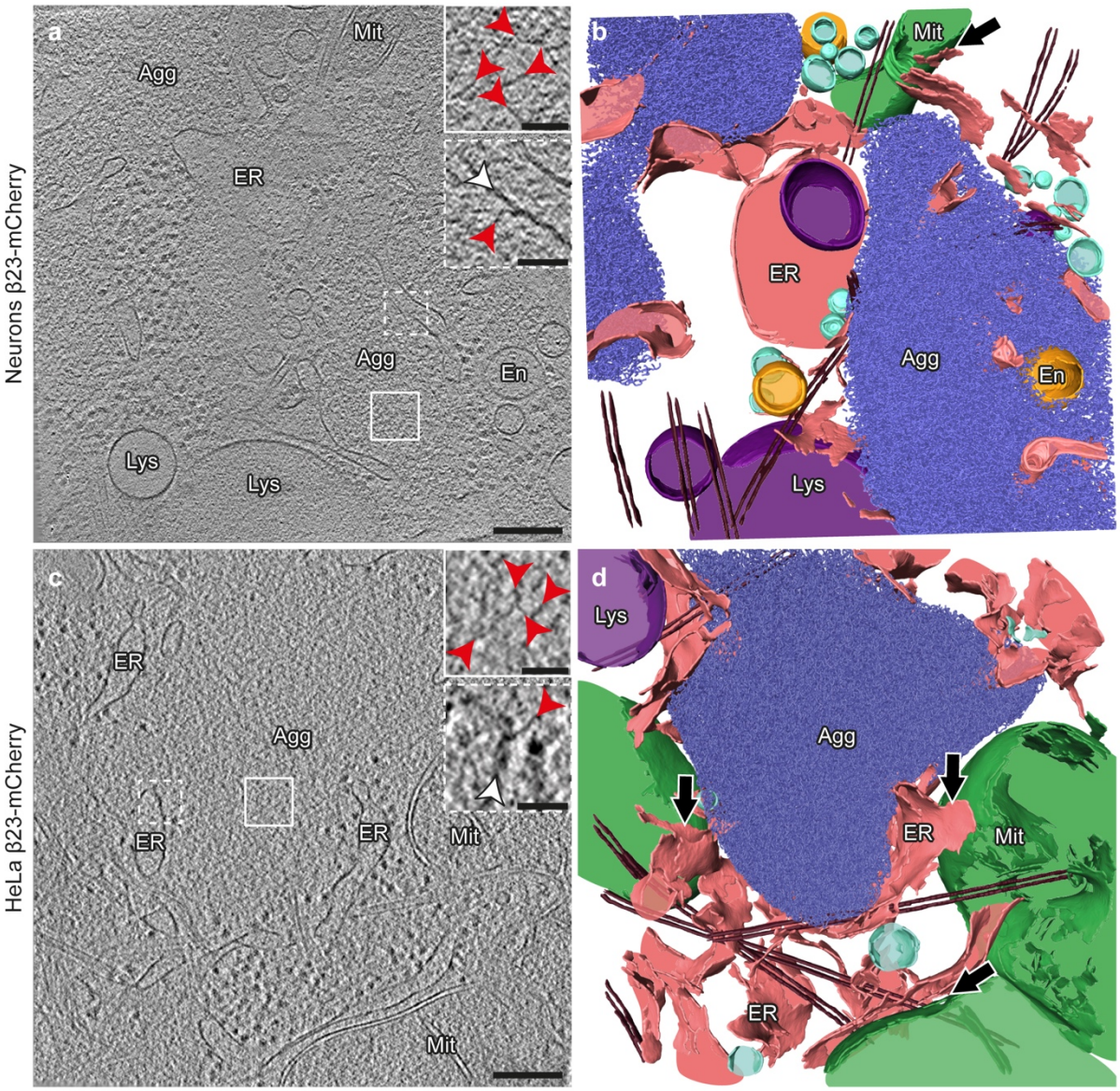

Supplementary Figure S3. Comparable aggregate morphology and cellular interactions in neurons and HeLa cells. Tomograms of β23-mCherry aggregates in primary neurons (**a**) and HeLa cells (**c**). Red arrowheads point to β23 fibrils (insets). White arrowheads point to intracellular membranes (lower insets). Agg, β protein aggregate; En, endosome; ER, endoplasmic reticulum; Lys, lysosome; Mit, mitochondrion. **b**, **d**, 3D rendering of the tomograms shown in **a** and **c**, respectively. ER membranes are found in close proximity to both aggregates and mitochondrial and lysosomal membranes. Black arrows indicate ER - mitochondria contact sites. β23-mCherry fibrils, blue; mitochondria, green; ER membranes, salmon; endosomes, gold; lysosomes, purple; vesicles, cyan; microtubules, brown. Scale bars in **a** and **c**, 200 nm and 50 nm (insets).

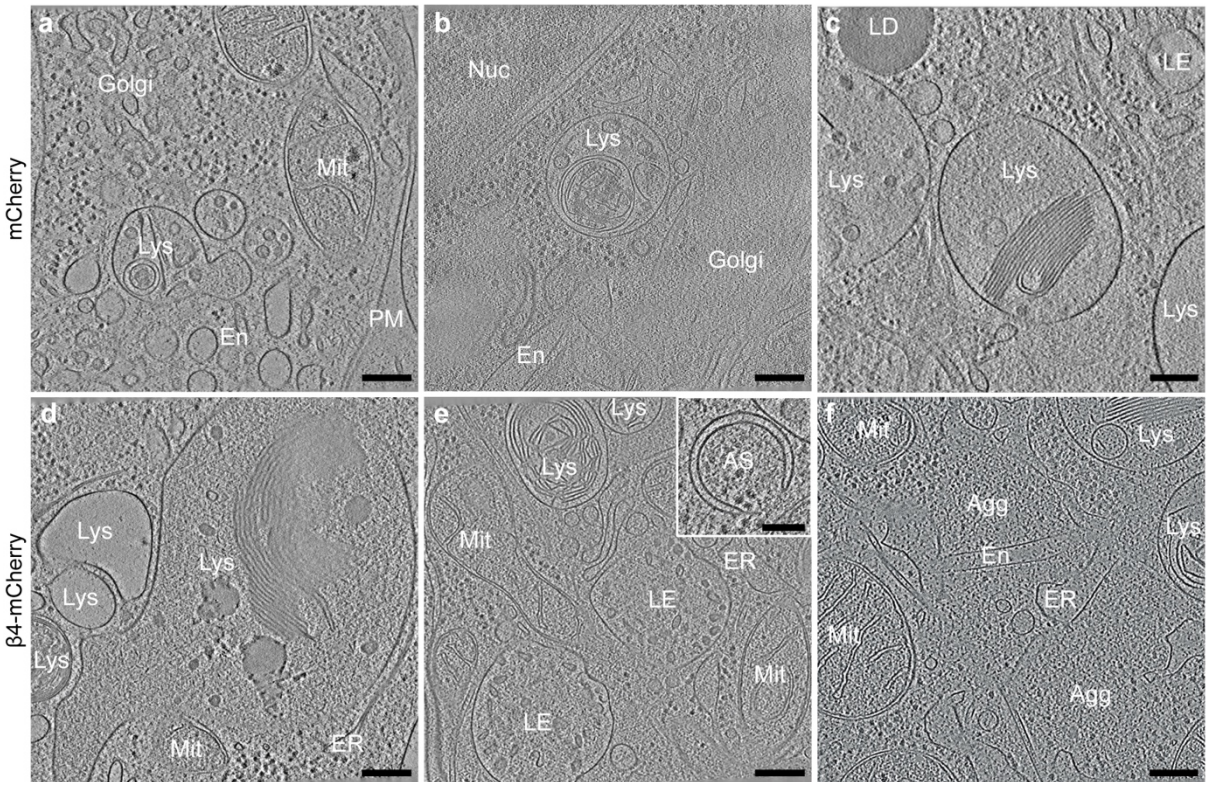

Supplementary Figure S4. Gallery of lysosomal morphologies. Tomograms from neurons transfected with mCherry (**a-c**) and β4-mCherry (**d-f**). Note that in cells with β protein aggregates, lysosomes often contain extensive stacks of membranes (**d-f**). Inset in **e** shows an example of an early autophagosome. Agg, β protein aggregate; AS, autophagosome; En, endosome; ER, endoplasmic reticulum; LD, lipid droplet; LE, late endosome; Lys, lysosome; Mit, mitochondrion; PM, plasma membrane. Scale bars in **a-f**, 200 nm; inset in **e**, 100 nm.

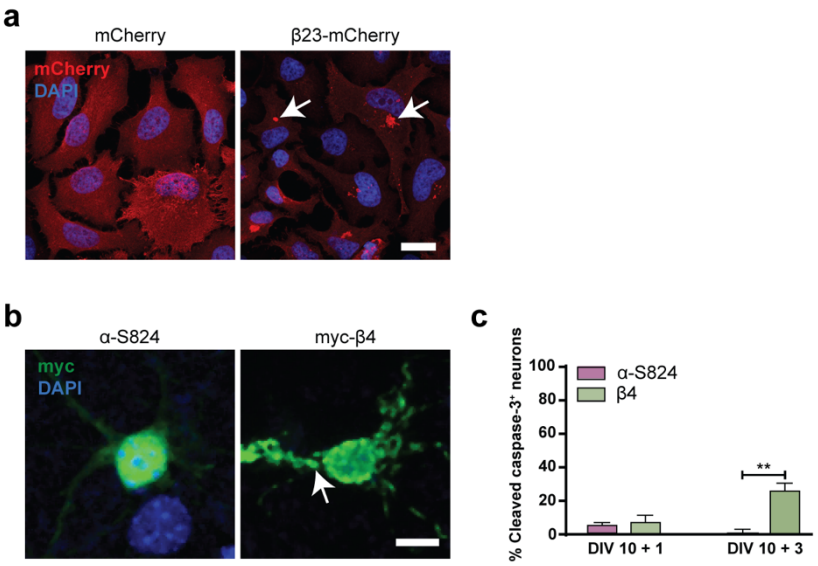

Supplementary Figure S5. Expression of β23-mCherry in HeLa cells and myc-β4 in primary neurons. a, HeLa cells transfected with mCherry or β23-mCherry (red). Nuclei were labeled with DAPI (blue). Arrows point to β23-mCherry aggregates. **b**, Examples of DIV 10+1 cortical neurons transfected with the indicated constructs and stained against myc (green). Nuclei were labeled with DAPI (blue). Arrow points to aggregated myc-β4. **c**, Quantification of the fraction of transfected neurons positive for cleaved caspase-3 at the indicated time points (n=2 independent cultures at DIV 10+1 and 3 independent cultures at DIV 10+3; 15-50 cells/condition/experiment; Two-way ANOVA with Bonferroni post hoc test). **p<0.01. Scale bars: 50 μm in **a**; 10 μm in **b**.

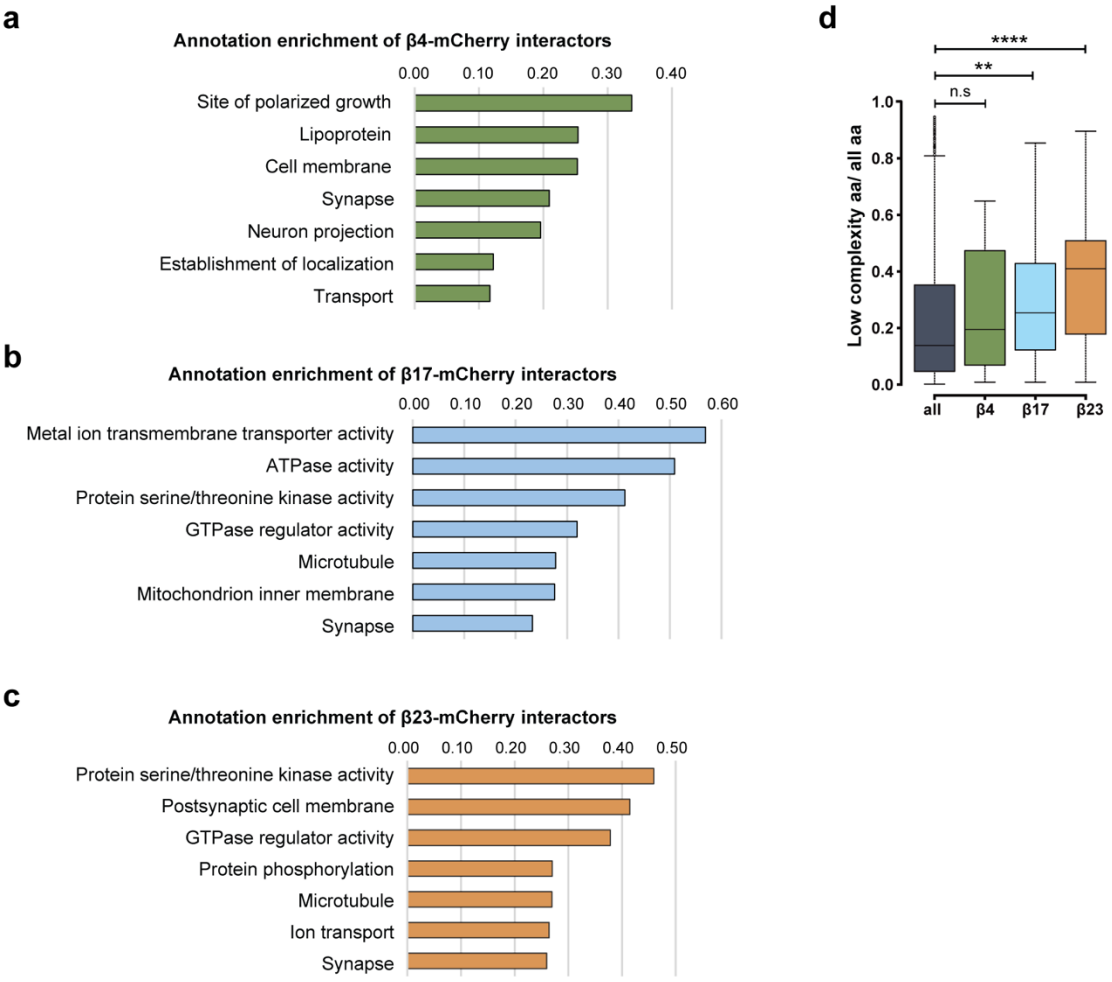

Supplementary Figure S6. GO annotations and bioinformatic characterization of β protein interactors. a-c, Pathway enrichment analysis of interactors of β4-mCherry (**a**), β17-mCherry (**b**) and β23-mCherry (**c**). **d**, Box plots of low complexity regions content in all identified proteins and in β protein interactors (n=4 independent experiments; Two-sample Wilcoxon test). **p<0.01; ****p<0.0001; n.s. – not significant.

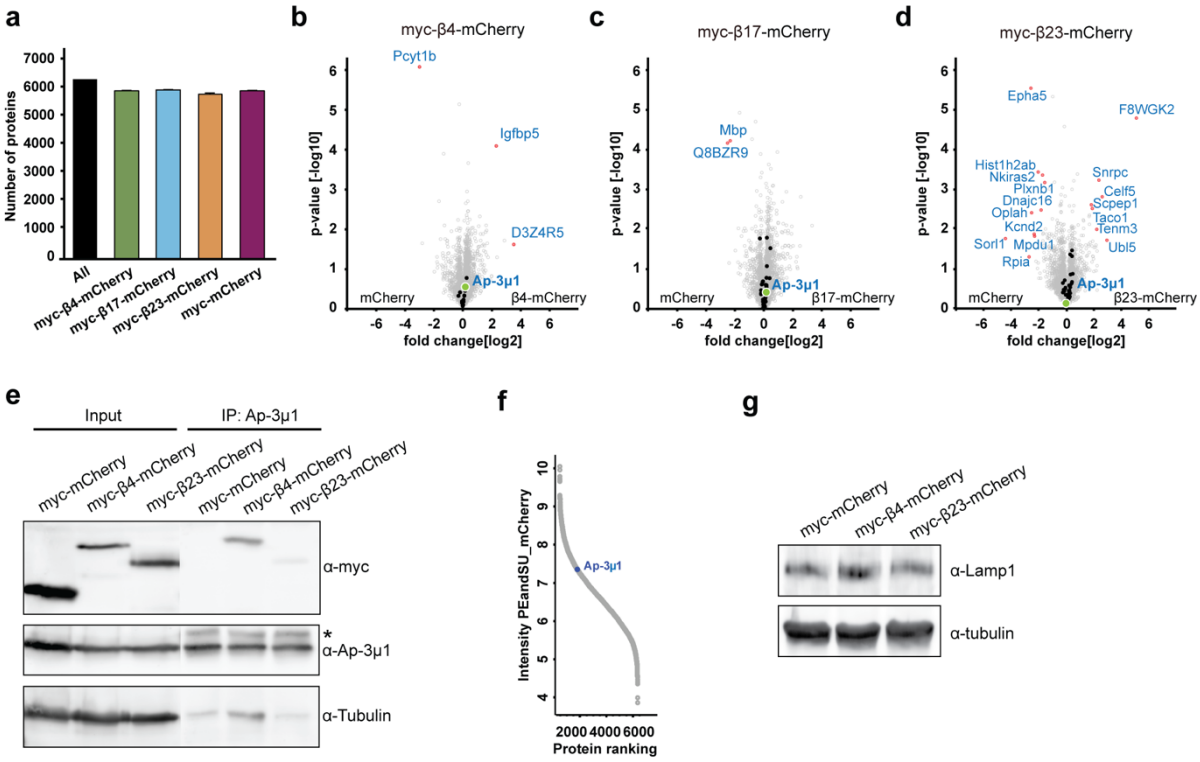

Supplementary Figure S7. Total proteome of β protein-expressing neurons. a, Numbers of identified proteins in all conditions together, and in neurons transduced with the indicated constructs (n=4 independent experiments). **b-d**, Volcano plots of the total proteome of β protein compared to mCherry neurons. Significantly regulated proteins are shown in red; Interactors of the respective β protein in black; AP-3µ1 is highlighted in green. **e**, Co-immunoprecipitation of β proteins with endogenous AP-3µ1. Lanes on the blot between input and IP were digitally removed. Asterisk marks IgG heavy chain band. **f**, Abundance ranking of all identified proteins in the whole proteome. AP-3µ1 (indicated in blue) is at position 1,296. **g**, Western blot of for endogenous Lamp-1 in lysates of primary neuronal cultures transduced with the indicated constructs. Tubulin was used as a loading control. β4-mCherry, 105.25 ± 37.2% of control; β4-mCherry, 104.8 ± 22.8% of control; n=2 independent experiments.

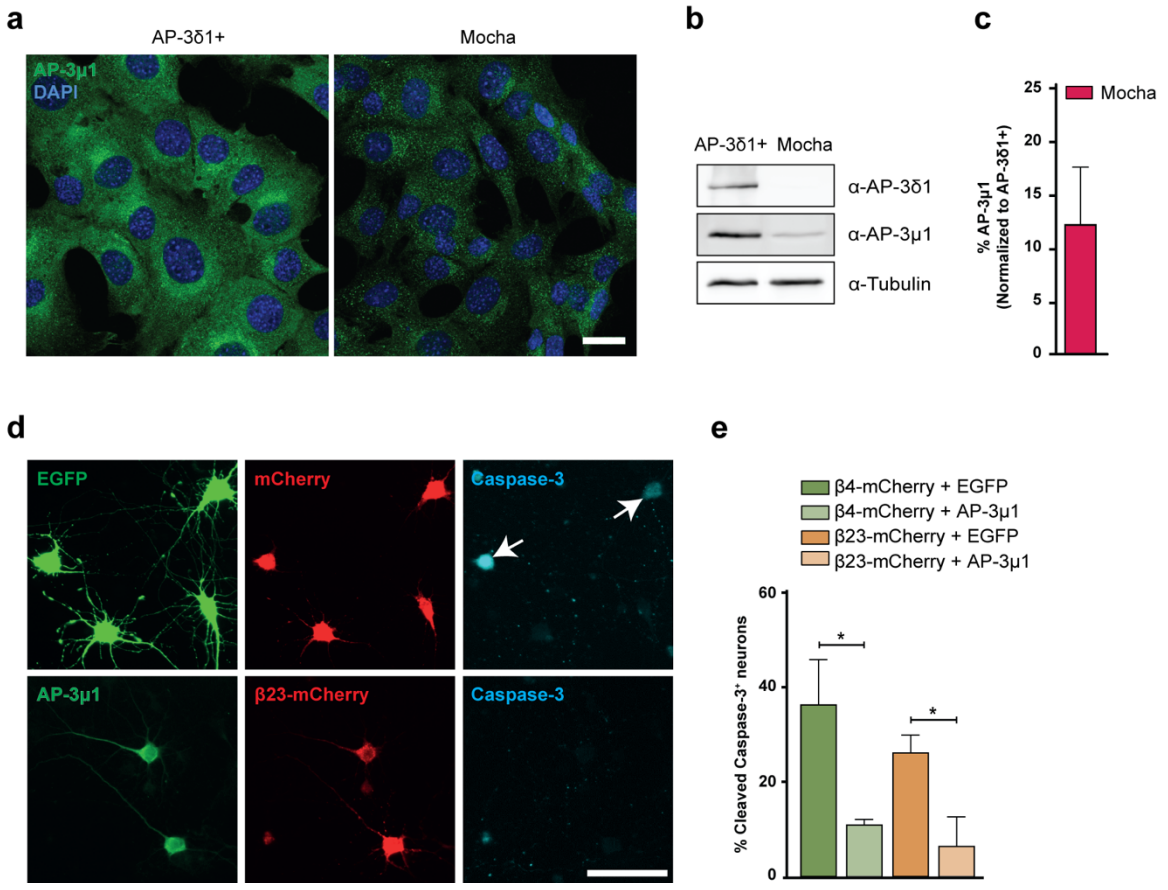

Supplementary Figure S8. AP-3µ1 levels are reduced in mocha cells, and overexpression of AP-3µ1 rescues β protein toxicity in neurons. a, Fluorescent images of control (left) and mocha cells (right) immunostained for AP-3µ1 (green). Nuclei were labelled with DAPI (blue). **b**, Western blots for the indicated AP-3 subunits. Tubulin was used as loading control. **c**, Quantification of AP-3µ1 protein levels in mocha cells. Values were normalized to control cells (n=3 independent experiments). **d**, Examples of cleaved caspase-3 staining in DIV 6+1 cortical neurons co-transfected with β23-mCherry and either EGFP (top) or AP-3µ1 (bottom). Anti-Flag staining was used to detect AP-3µ1. Arrows point to cleaved caspase-3 positive cells. **e**, Percentage of double-transfected neurons positive for cleaved caspase-3 (n=3 independent experiments; 10-60 cells/condition/experiment; Two-tailed t-test). *p<0.05. Scale bars: **a**, 20 µm; **d**, 50 µm.

Supplementary Tables

Supplementary Table S1. Statistics of cryo-ET experiments.

Data analyzed	Cell type	Condition	Number of experiments	Number of cells	Number of observations
Aggregates	Neurons	β4-mCherry	3	9	21
	Neurons	β23-mCherry	2	2	4
	HeLa	β23-mCherry	4	7	23
Lysosomes analyzed for aggregate content	Neurons	β4-mCherry	5	10	38
	Neurons	β23-mCherry	3	5	31
Early autophagosomes	Neurons	mCherry	5	14	1
	Neurons	β4-mCherry	5	15	2
	Neurons	β23-mCherry	4	9	0

Supplementary Table S2. β protein interactors and proteins significantly changed in the total proteome.

Supplementary Table S3. Total proteome of primary neurons expressing β proteins.